Magneto-thermal Transport and Machine Learning-assisted Investigation of Magnetic Materials

by

Yuki Tatsumi

Submitted to the Department of Physics
in partial fulfillment of the requirements for the degree of

Master of Science in Physics

at the

MASSACHUSETTS INSTITUTE OF TECHNOLOGY

Spetember 2021

Author .....
Department of Physics
August 5, 2021

Certified by .....
Joseph Checkelsky
Associate Professor
Thesis Supervisor

Accepted by .....
Deepto Chakrabarty
Associate Department Head of Physics

Magneto-thermal Transport and Machine Learning-assisted Investigation of Magnetic Materials

by

Yuki Tatsumi

Submitted to the Department of Physics
on August 5, 2021, in partial fulfillment of the
requirements for the degree of
Master of Science in Physics

Abstract

Heat is carried by different types quasiparticles in crystals, including phonons, charge carriers, and magnetic excitations. In most materials, thermal transport can be understood as the flow of phonons and charge carriers; magnetic heat flow is less well-studied and less well understood.

Recently, the concept of the flat band, with a vanishing dispersion, has gained importance. Especially in electronic systems, many theories and experiments have proven that some structures such as kagome or honeycomb lattices hosts such flat bands with non-trivial topology. Even though a number of theories suggest that such dispersionless mode exist in magnonic bands under the framework of the Heisenberg spin model, few experiments indicate its existence. Not limited to these flat band effects, magnetic insulators can assume a variety of nontrivial topologies such as magnetic skyrmions. In this thesis, I investigate the highly frustrated magnetic system $Y_{0.5}Ca_{0.5}BaCo_4O_7$, where the kagome lattice could potentially lead to nontrivial thermal transport originated from its flat band. While we do not observe signatures of the flat band in thermal conductivity, the observed anomalous Hall effect in electrical transport and spin glass-like behavior suggest a complex magnetization-transport mechanism.

Motivated by the rapid advancement of artificial inteligence, the application of machine learning into materials exploration is recently investigated. Using a graphical representation of crystallines orginally suggested in Crystal Graphical Convolutional Neural Network (CGCNN), we developed the ML-asssited method to explore magnetic compounds. Our machine learning model can, so far, distiguish ferromagnet or antiferromagnet systems with over 70% accuracy based only on structual/elemental information. Prospects of studying more complex magnets are described.

Thesis Supervisor: Joseph Checkelsky
Title: Associate Professor

Contents

List of Figures

Chapter 1

Chapter 2

Chapter 3

Chapter 1

Thermal conductivity in crystals

1.1 Introduction

Thermal conductivity is a measure of how heat is transported in a material. The roles of thermally conductive materials are diverse in society: high thermal-conductive heat sinks, for instance, are used in computers to release the heat generated in the CPU while aerogels are useful as insulation due to their low thermal conductivity. In condensed matter research, the underlying mechanism of thermal conduction is usually understood by the propagation of electrons/holes and the atomic vibration (phonons). However, some compounds possess another type of heat mediator, magnons, which represent the collective behavior of spins in a crystal. It is not always straightforward to identify the microscopic mechanism of heat conductivity. One reason is each quasiparticle is not completely independent of each other but creates new quasiparticles by their mutual interactions. Also, the magnitude of the contribution from some quasiparticles to the net thermal conductivity is so small that it is not detectable by typical transport probes. Owing to these complexities, not only thermal conductivity experiments but also neutron scattering measurements or electrical transport data are often necessary to understand heat transport in a given system. Below, we begin by discussing the theoretical background of thermal conductivity for phonons, electrons, and magnons.

1.2 Thermal conductivity by phonons and electrons

The thermal conductivity of a lattice can be understood by the kinetic approach. For simplicity, we consider a monoatomic Bravis lattices, where the phonon spectrum has only acoustic branches. Since we are concerned with qualitative features of thermal conduction, we shall also make the Debye approximation, letting the phonon dispersion relation be $\omega = ck$ for all three acoustic branches, where ω is the angular frequency, c is the wave's speed and k is the wavenumber. Suppose a small temperature gradient is imposed in the x-direction in an electrically insulating crystal. We assume the Drude model so that collisions maintain local thermodynamic equilibrium in a simple manner. Those phonons emerging from collisions at position x are taken to contribute to the nonequilibrium energy density an amount proportional to the equilibrium energy density at density temperature $u(x) = u^{eq}[T(x)]$. Each phonon at a given point will contribute to the thermal current density in the x-direction an amount equal to the product of the x-component of its velocity with its contribution to the energy density. However, the average contribution of a phonon to the energy density depends on the position of its last collision. Thus, there is a correlation between where a phonon comes from and its contribution to the average energy, which results in a net thermal current.

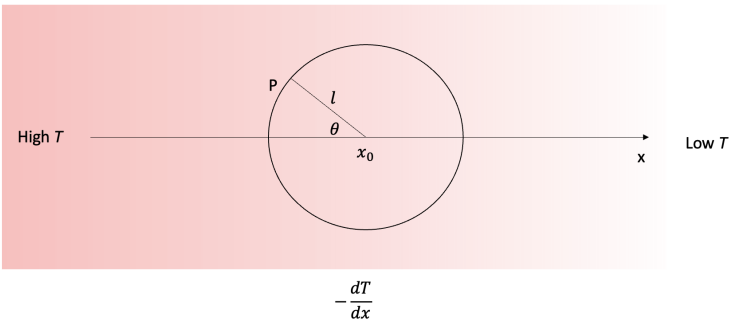

Figure 1-1: Heat propagation by phonons in the presence of a uniform temperature gradient along the x-axis. Each variables is defined assuming the collision occurred a distance $l = c\tau$ from the point x_0, in a direction making an angle θ to the x-axis.

To estimate this thermal current j, we average the product of the energy density and the x-velocity over all the places where the phonon's last collision might have occurred. Figure 1-1 shows the schematic of a collision of two phonons at x_0 in one dimesional space. Assuming, in the spirit of the Drude model, that the collision occurred a distance $l = c\tau$ from the point x_0, in a direction making an angle θ to the x-axis we have

$$\begin{aligned} j &= < c_x u(x_0 - l\cos\theta) >= \int c\cos\theta u(x_0 - l\cos\theta)\frac{2\pi d\theta}{4\pi}\sin\theta, & (1.1)\\ &= \frac{1}{2}\int \mu d\mu c u(x_0 - l\mu) & (1.2) \end{aligned}$$

If we consider only the linear term $\frac{dT}{dx}$,

$$j = \kappa(-\frac{dT}{dx}) \tag{1.3}$$

where the thermal conductivity κ is given by

$$\kappa = \frac{1}{3}c_v c l = \frac{1}{3}c_v c^2 \tau \tag{1.4}$$

Here c_v is the specific heat of the phonons and is one of the quantities that determines the temperature dependence of κ. The other is the phonon collision rate τ^{-1}. The collision rate is not straightforward to characterize in general, but we can discuss the following two limits with respect to the Debye temperature θ_D:

Case 1: ($T >> \theta_D$) At high temperatures the total number of phonons present in the crystal is proportional to T because the thermal equilibrium phonon occupation numbers reduce to

$$n(k) = \frac{1}{e^{\frac{\hbar\omega(k)}{k_B T}} - 1} \approx \frac{k_B T}{\hbar\omega(k)} \tag{1.5}$$

Since a given phonon that contributes to the thermal current is more likely to be scattered the more other phonons there are present to do the scattering, we should expect

the relaxation time to decrease with increasing temperature. Furthermore, since at high temperature the heat capacity is independent of temperature, it is expected that the thermal conductivity itself is decreasing with increasing temperature. Thus, we find,

$$\kappa \propto \frac{1}{T^x} \tag{1.6}$$

Case 2: ($T << \theta_D$) At any temperature T, only phonons with energies comparable to or less than $k_B T$ will be present in appreciable numbers. In particular, when $T << \theta_D$, the phonons present will have $w(k) << \omega_D$, and $k << k_0$, where $k_B \theta_D = \frac{\hbar}{k_B} \omega_D$ and k_0 is given below. With this in mind, we consider a phonon collision mediated by the cubic or quartic anharmonic terms. Since only a small number of phonons are involved, the total energy and total crystal momentum of those phonons that participate in the collision must be small compared with $\hbar$ and k_0. Since energy is conserved in the collision, the total energy of the phonons emerging from the collision must continue to be small compared with $\hbar\omega$. This is only possible if the wave vector of each, and hence their total wave vector is small compared with k_0. However, both initial and final total wave vectors can be small compared with k_0 (the Umklapp process) only if the additive reciprocal lattice vector k appearing in the crystal momentum conservation law is zero. Thus, at very low temperatures, the only collisions occurring with appreciable probability are those that conserve the total crystal momentum exactly, and not just within an additive reciprocal lattice vector. This Umklapp process represents backscattering, indicating a reduction to the net thermal conduction. The number of phonons that can participate in the Umklapp processes drops exponentially as temperature drops. Without the Umklapp processes, the thermal conductivity would be infinite, and we, therefore, expect that the effective relaxation time appearing in the thermal conductivity must vary as

$$\tau \propto e^{\frac{T_0}{T}} \tag{1.7}$$

where T is well below θ_D and the order of T_0 is at θ_D.

Combining those two temperature limits, the temperature dependence of thermal conductivity is understood as shown in Figure 1-2. When the temperature reaches a point where the exponential increase in the thermal conductivity sets in, the conductivity increases so rapidly with decreasing a temperature that the phonon mean free path soon becomes comparable to the mean free path due to the scattering of phonons by lattice imperfections or impurities, or even to the mean free path describing the scattering of phonons by the sides of the finite specimen. Once this happens, the mean free path ceases to be the intrinsic one due to anharmonic terms, and must be replaced by a temperature-independent length determined by the spatial distribution of imperfections or the size of the specimen. The temperature dependence of κ then becomes that of the specific heat, which declines as T^3 at temperatures well below θ_D.

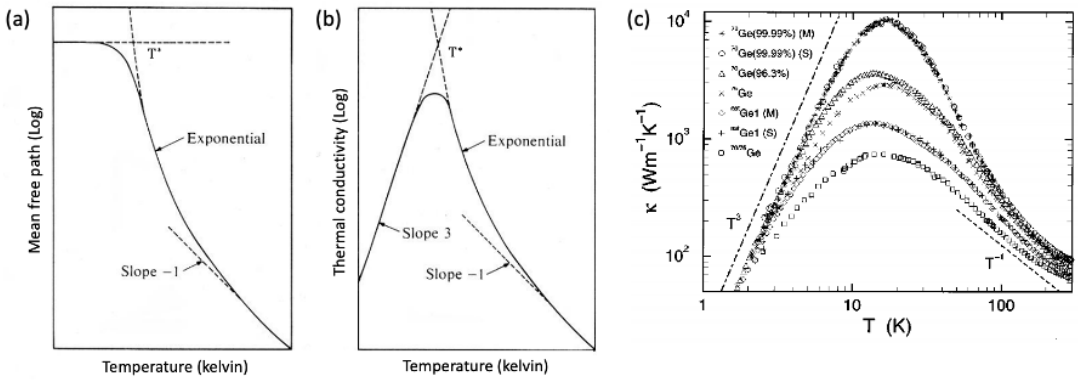

Figure 1-2: (a),(b) Typical temperature dependence of phonon mean free path and thermal conductivity, respectively. (c) An example of experimental thermal conductivity: temperature dependence of the thermal conductivity of Ge samples with different isotopic compositions. All figures are from [1].

In the thermal conductivity of a metal, the Wiedemann-Franz law states that the ratio, κ/σ, of the thermal to the electrical conductivity is directly proportional to the temperature. The ratio is approximately constant over many metals and is given within the regime of kinetic theory. The kinetic thermal conductivity of electrons κ_e

is given by

$$\kappa_e = \frac{1}{3} c_e v l = \frac{1}{3} c_e v^2 \tau \tag{1.8}$$

where c_e, v, l and τ are specific heat, velocity, mean free path of electrons, respectively. Since the DC conductivity in Drude model is $\sigma = \frac{ne^2\tau}{m}$, the Wiedemann-Franz ratio is given within the regime of kinetic theory. The kinetic thermal conductivity of electrons is given by

$$\frac{\kappa_e}{\sigma} = \frac{c_e m_e v^2}{ne^2} \tag{1.9}$$

By taking the Fermi sphere, the specific heat $c_e = \frac{\pi^2}{2}(\frac{k_B T}{\epsilon_F})nk_B$ and electron velocity (fermi velocity) $v_F^2 = \frac{2\epsilon}{m}$ yields to

$$\frac{\kappa_e}{\sigma T} = \frac{\pi^2 k_B^2}{3e^2} = 2.4 \times 10^{-8} \mathrm{W\Omega/K^2} \tag{1.10}$$

1.3 Magnon heat transport

In a magnetically ordered crystal the propagating excitation of the spin system, known as magnons, can transport heat in a manner analogous to the more familiar lattice excitations. It was suggested early on that, at a few hundred Kelvin, the heat transport by collective excitations of coupled paramagnetic ions might exceed that transported by phonons. On the other hand, in a ferromagnetic dielectric, where spins are strongly coupled to their neighbors, the spin-wave heat transport is most relevant at few K. In this range, the magnon systems can have a specific heat equal to or greater than that of the phonons. The velocities of the excitations are comparable, and at sufficiently low temperatures their mean free paths are equal since both are limited only by the boundaries of the sample. Thus, a large fraction of the thermal conductivity could be due to the magnons. In the most simple case, magnon conductivity has been recognized by a deviation of the thermal conductivity from T^3 behavior expected for typical phonon conduction behavior as described above [10, 11]. One of the most

well-known systems of magnon conduction is observed in ferrimagnetic yttrium iron garnet (YIG)[12].

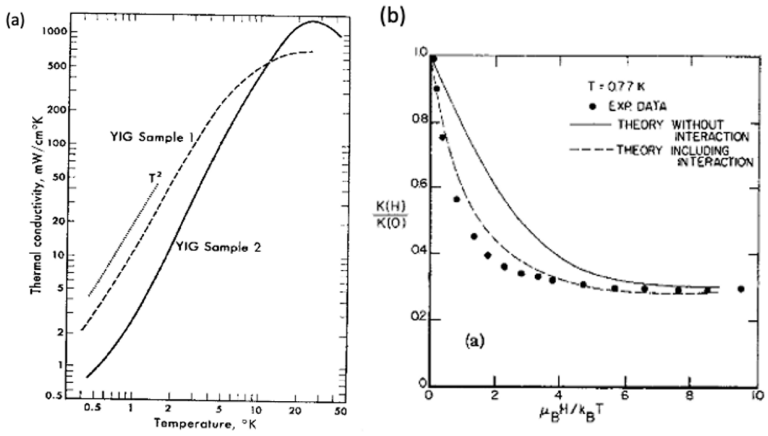

Figure 1-3: (a) Temperature dependence of the thermal conductivity of yttrium-iron-garnet in log scale. From [2]. (b) The relative decrease of the thermal conductivity of YIG in an external magnetic field. The drawn lines correspond to different theoretical calculations from [3].

The thermal conductivity of YIG exhibited the expected dependence on the temperature and magnetic field as shown in Figure 1-3. At low-temperature the conductivity is nearly proportional to T^2. By measuring the conductivity in magnetic fields that are large enough to remove the magnon contribution completely, it was estimated that about two-thirds of the zero-field conductivity was due to the magnons. Not only does the thermal conductivity decrease with increasing the field, but it also saturates in high fields. The thermal conductivity decrease in the field can be also due to phonons, because an external field changes the energy of magnons and phonons. It is shown that the magnetic field dependence of the thermal conductivity of yttrium iron garnet can be accounted for if the coupled magnon-phonon modes are present.

We have studied thermal conduction behavior in magnetically frustrated systems, in particular where the magnonic flat band resides in zero energy. The kagome lattice in a quantum magnetic system tends to support exotic transport phenomena; several Cu-Kapellasites have the transverse component of thermal conductivity originating

from their non-trivial spin texture [13] [14]. On the other hand, the classical magnetic kagome system also remains one of the most interesting platforms where the large manifolds of magnon states caused by its characteristic geometric structure create a flat magnonic band. Even though such a flat band is confirmed in Co-based kagome magnet, $Y_{0.5}Ca_{0.5}BaCo_4O_7$, by inelastic neutron experiments, there has not been any direct observation of its consequences in transport experiments. We conduct thermal transport experiments along with electrical transport measurements to understand the nature of this classical kagome magnet.

This thesis consists of the following: the 2nd and 3rd chapters describe the experimental approach and results of thermal conductivity in frustrated systems. In the 4th chapter, we study possible machine learning-assisted exploration of magnetic materials. In the 5th chapter, we provide a summary and outlook.

Chapter 2

Experimental methods

2.1 Sample prepation

This chapter presents the techniques used in crystal growth of $Y_xCa_{1-x}BaCo_4O_7$. Samples studied in this thesis and its preparation methods are listed in Table 2.1. $Y_{0.5}Ca_{0.5}BaCo_4O_7$, $CaBaCo_4O_7$, and $YBaCo_4O_7$ are prepared as both single crystals by the Optical Floating Zone method (FZ) and polycrystals by solid state reactions (SS).

Sample	type	method	conditions
$Y_{0.5}Ca_{0.5}BaCo_4O_7$	Single crystal	FZ	0.2 O_2 0.8 Ar gas pressurized
$Y_{0.5}Ca_{0.5}BaCo_4O_7$	Polycrystal	SS	Quench at 700°C
$YBaCo_4O_7$	Single crystal	FZ	0.2 O_2 0.8 Ar gas
$YBaCo_4O_7$	Polycrystal	SS	Quench at 700°C
$CaBaCo_4O_7$	Single Crystal	FZ	0.2O_2 0.8 Ar gas pressurized
$CaBaCo_4O_7$	Polycrystal	SS	Quench at 700°C

Table 2.1: The series of compounds $Y_xCa_{1-x}BaCo_4O_7$ synthesized in this study.

2.1.1 Optical Floatng Zone Method

The single-crystal samples listed in Table 2.1 were synthesized from the powder obtained by quenching and then melted using a floating zone furnace. Powder with a stoichiometric composition is pressed into a rod, to be used as a seed, and also as a feeding rod. The schematic of the setup is shown in Figure 2-1. Growth in a floating zone furnace is done inside a pressurized quartz cylinder. The seed rod is set on the bottom and the feed rod is set on the top and is set to rotate around its axis. By moving the rods closer to the focus point of the radiative heaters a melted zone between the rods is achieved. The rods are slowly moved down to change the temperature gradient in the material, which crystallizes the material at the end of the seed rod.

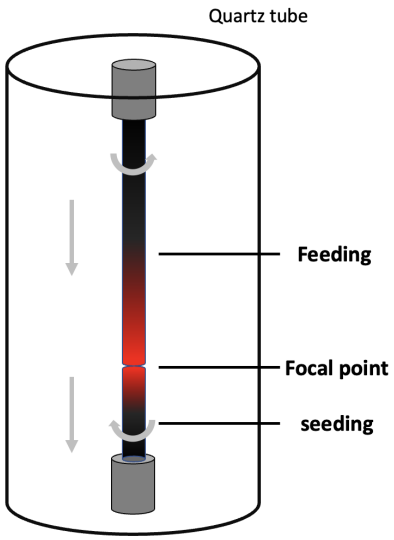

Figure 2-1: Schematic of the floating zone furnace: the radiative heating is used to melt the zone at the focal point from the four lumps. The growth is done under the pressurized environment.

The sample rod of the floating zone method is typically 4 to 8 cm long as shown in Figure 2-2. The growth speed is from 0.2 to 1.5 mm/sec. Figure 2-3 shows a piece of a single crystal cut out from the rod with a diamond cutter.

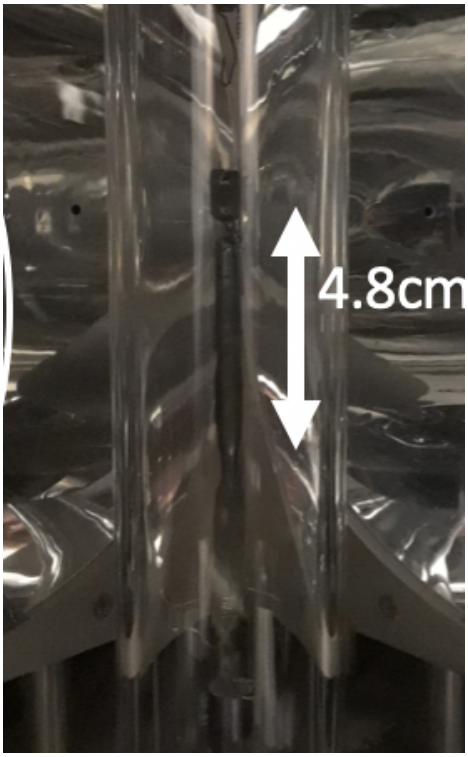

Figure 2-2: The rod produced by the floating zone method. The compositions of the feeding and seeding rods are the stoichiometric sintered compounds of $Y_{0.5}Ca_{0.5}BaCo_4O_7$.

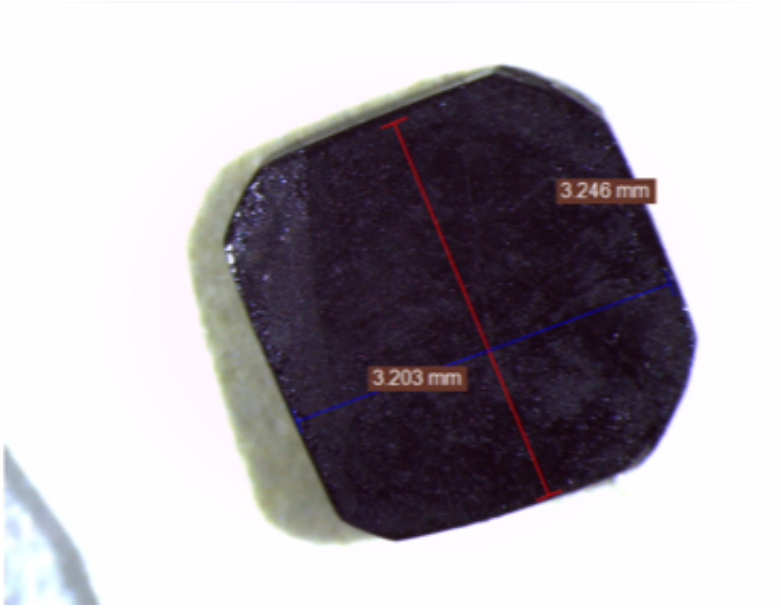

Figure 2-3: Single crystal separated from the original rod from Figure 2-2.

2.2 Crystalline sample evaluation

Crystalline solids are studied by the means of diffraction of electrons, neutrons, and photons to characterize their crystal structure, mechanical and magnetic properties. This chapter presents the theory of the diffraction of waves by crystals.

2.2.1 Diffraction of waves from crystals

To understand the x-ray diffraction and neutron scattering experiments, as well as the structure factor calculations, an introduction to wave diffraction by crystals is required. Waves with wavelength much greater than the interatomic spacing incident on a solid follow optical reflection and refraction relations. When the wavelength is of the same order as the interatomic spacing in the solid, diffraction must be considered. Suppose a wave with wave vector k is incident on two differential volumes separated by a distance r, and the outgoing wave vector k'. The angle between k and k' is denoted 2θ. For the incident wave, the difference in path length between the two points is $r \sin\theta$, so the phase difference is $k \cdot r$. Similarly, the phase difference coming

from the diffracted portion is $-k' \cdot r$. Therefore the phase factor can be written as $exp[i(k - k') \cdot r]$. Assuming that the amplitude of the scattered wave from the differential volume is proportional to the electron density, the total amplitude is then given by the integral,

$$F = \int_{crystal} n(r) exp(-iG \cdot r) dV = NS_G \tag{2.1}$$

where S_G is called the structure factor, and r can be chosen to be zero at one corner of the cell. Suppose the cell contains s atoms that contribute to the electron density at r such that $n(r) = \sum n_j(r - r_j)$ where n_j is the contribution of the jth atom $j = 1$ located at r_j. Then the structure factor is given by

$$S_G = \sum f_j exp(-iG \cdot r_j) \tag{2.2}$$

where

$$f_j = \int n_j(r_0) exp(-iG \cdot r_0) dV \tag{2.3}$$

f_j is an atomic property and depends on the type of scattering experiment considered. For x-rays, the form factor is not very sensitive to small redistributions of the electrons in comparison to a free atom, and thus it is close to the form factor for electrons localized at the atom, giving the simple form $f_j = Z$ where Z is the atomic number.

2.2.2 X-ray powder diffraction

The PANalytical X'Pert Pro Multipurpose Diffractometer is used to determine the phases in a sample of this study. The powderized samples before and after the floating zone are evaluated with x-ray measurements (see Figure 2-4). The blue peaks are the calculated values from a previous report [15], and are consistent with the observed signals of this study.

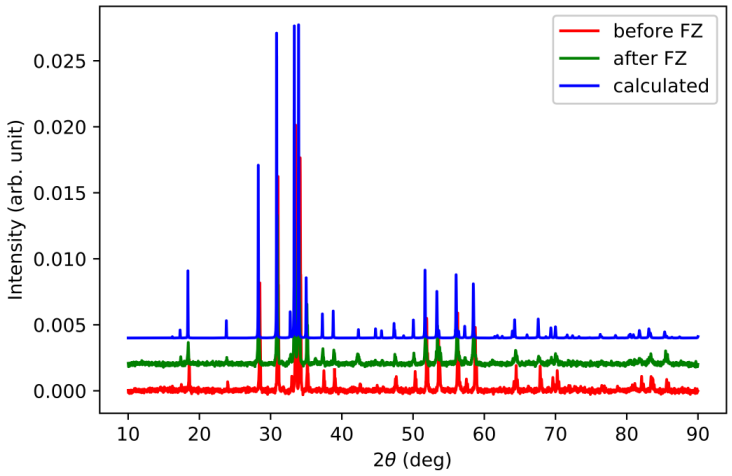

Figure 2-4: Powder x-ray measurement of powder, single crystal, and calculated value of $Y_{0.5}Ca_{0.5}BaCo_4O_7$.

2.2.3 Laue back scattering

The Laue x-ray measurement is used to align a single crystal. Figure 2-5 is the Laue pattern of the piece of the crystal shown in the Figure 2-3, which indicates that this piece of crystal is the large single domain with the c-axis is out of the page direction.

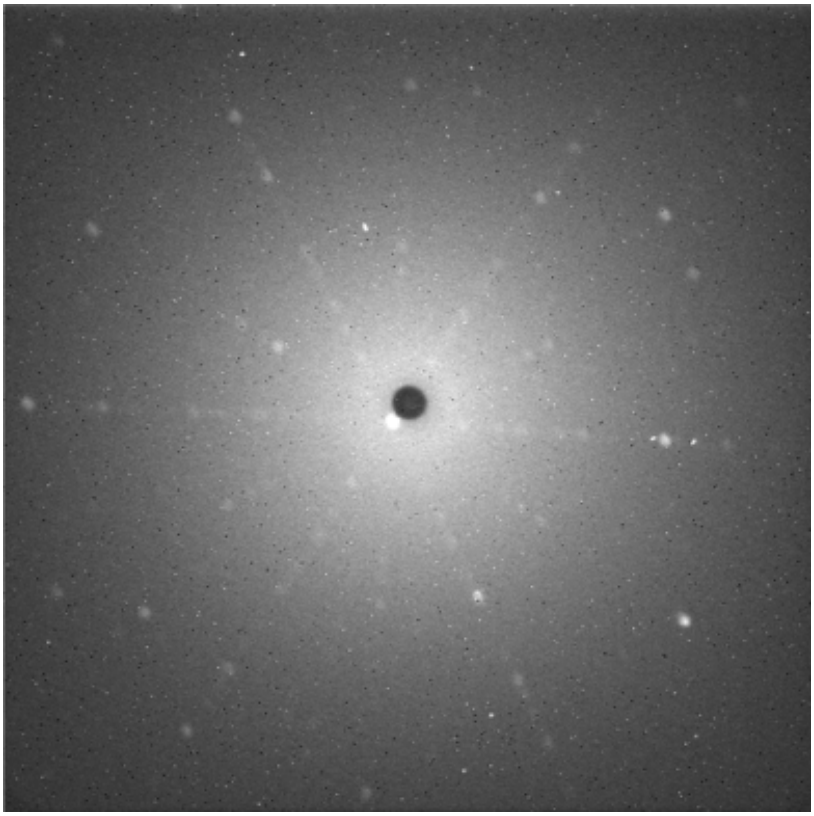

Figure 2-5: Laue x-ray backscattering measurement of the single crystal of $Y_{0.5}Ca_{0.5}BaCo_4O_7$.

2.3 Magnetization and electric transport measurements

Magnetization and electronic transport properties were measured by use of Magnetic Property Measurement System (Quantum Design) and Physical Property Measurement System (Quantum Design). A conventional four-terminal method was used for the resistivity measurement. Typical size of the samples are $1 \times 0.5 \times 0.5$ mm^3 for $Y_{0.5}Ca_{0.5}BaCo_4O_7$ and $1.5 \times 1.5 \times 0.5$ mm^3 for $CaBaCo_4O_7$ and $YBaCo_4O_7$. We used Indium as a contact adhesive to reduce contact resistances. We removed the anisotropic biases from the longitudinal resistivity $\rho_{xx}(\mu_0 H)$ and calculated antisym-

metric component $\rho_{yx}(\mu_0 H)$ of the Hall resistivity by the following equations.

$$\rho_{xx}(\mu_0 H) = \frac{\rho_{xx}^{exp}(\mu_0 H) + \rho_{xx}^{exp}(-\mu_0 H)}{2}, \tag{2.4}$$

$$\rho_{yx}(\mu_0 H) = \frac{\rho_{yx}^{exp}(\mu_0 H) - \rho_{yx}^{exp}(-\mu_0 H)}{2} \tag{2.5}$$

where H is applied magnetic field and μ_0 is magnetic permeability in vaccum.

In the magnetization measurements, crystal rods are used as the mounting stage and powder samples are put in a capsule. Magnetization was measured as a function of temperature over the range 2 K - 350 K at several applied fields ranging from 0 Oe to 70,000 Oe. Measurements were performed with the field applied both parallel and perpendicular to the kagome plane for single crystals. Measurements were performed under both field-cooled and zero-field-cooled conditions. Also, the isothermal measurements were performed under different temperature range with a variety of applied field magnitude.

2.4 Thermal transport and heat capacity measurements

2.4.1 Heat capacity measurement

Specific heat was measured by a commercial system. When the heat power Q is provided to the sample which is attached to the heat bath of the temperature T_{bath}, the following relation holds:

$$Q = \kappa(T - T_{bath}) + C\frac{dT}{dt} \tag{2.6}$$

where κ is the thermal conductance between the sample and the heat bath. The temperature difference between the sample and heat bath after the heater is switched

off and is expressed by the relaxation relation:

$$T - T_{bath} = (T_1 - T_{bath})exp(-\frac{t}{\tau}) \tag{2.7}$$

where T_1 is the temperature of the sample after time t passed since the heater was turned off. As a result, the heat capacity C can be estimated from the relaxation time τ by,

$$C = \kappa\tau. \tag{2.8}$$

2.4.2 Thermal conductivity and thermal Hall measurement

The schematic of the experimental setup for the thermal conductivity is shown in Figure 2-6. It consists of an electrical heater and thermocouples attached to a crystal mounted on a heat bath.

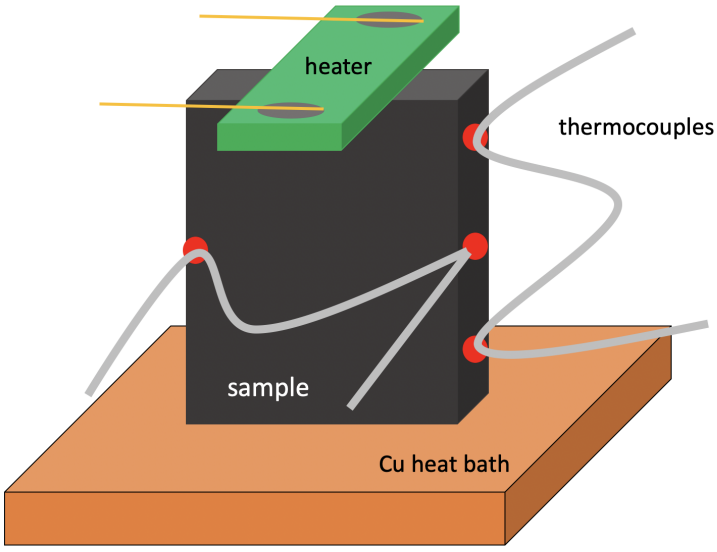

Figure 2-6: Experimental setup for thermal transport measurement.

The thermal conductivity tensor is the linear response about the heat current J_Q

across the sample to the temperature gradient ΔT:

$$J_Q = \bar{\kappa} \cdot (-\Delta T) = \begin{pmatrix} \kappa_{xx} & \kappa_{xy} \\ \kappa_{yx} & \kappa_{yy} \end{pmatrix} \cdot (-\Delta T) \tag{2.9}$$

and the thermal resistivity tensor is the inverse, $\bar{\omega} = \bar{\kappa}^{-1}$. Using these, the longitudinal thermal conductivity κ_{xx} and the thermal Hall conductivity κ_{xy} are obtained by the following relation:

$$\kappa_{xx} = \frac{\omega_{xx}}{\omega_{xx}^2 + \omega_{xy}^2} = -\frac{j_Q}{\frac{\partial T}{\partial x}}, \tag{2.10}$$

$$\kappa_{xy} = -\frac{\omega_{xy}}{\omega_{xx}^2 + \omega_{xy}^2} = \frac{\kappa_{xx}^2 \frac{\partial T}{\partial y}}{j_Q} \tag{2.11}$$

where j_Q is the density of J_Q. In the same way as the electric measurement, we extracted the longitudinal symmetric component and the transverse antisymmetric component of temperature gradient under the magnetic field. The modified temperature gradients are calculated as:

$$\frac{\partial T}{\partial x} = \frac{\Delta_x T(B) + \Delta_x T(-B)}{2l_x}, \tag{2.12}$$

$$\frac{\partial T}{\partial y} = \frac{\Delta_y T(B) - \Delta_y T(-B)}{2l_y} \tag{2.13}$$

where $\Delta_i T$ and d_i are the observed temperature difference and distance between thermometers in each direction (x: longitudinal, y: traverse). In semiconducting system as studied here the contribution from charged particles is small enough only to consider phononic and magnetic excitations.

Chapter 3

Thermal transport in kagome frustrated magnets

3.1 The Kagome lattice

In condensed matter physics, collective phenomena in strongly correlated electron system have attracted great interest. The collective behavior of electrons can be understood by the excitation of quasiparticles, which leads to exotic phenomena distinct from those of bare electrons [16]. We are particularly interested in the system whose structure (*e.g.* the geometry of the underlying crystal structure) is strongly correlated to their physical properties. The magnetic insulators are often understood by the spin localized picture. The kagome lattice, where the basis is arranged such that the lattice tiles the plane with corner-sharing triangles as shown in Figure 3-1, hosts many exotic behaviors.

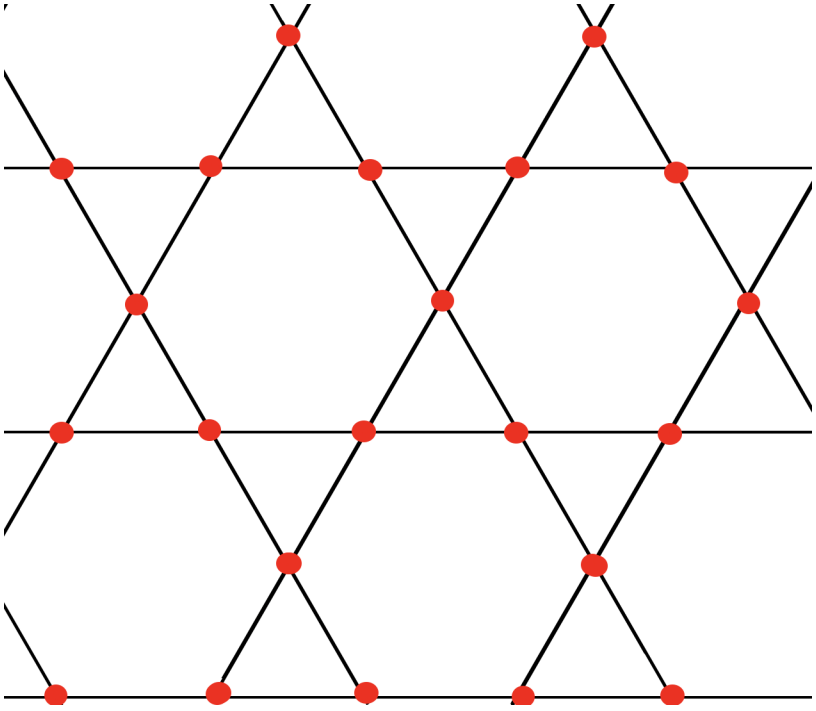

Figure 3-1: The kagome lattice.

In real materials, the crystal lattice is three-dimensional but often can be viewed as effectively two-dimensional if it consists of layers of kagome planes that are separated such that interactions between the layers are weak.

3.1.1 The Ferromagnet Kagome Lattice

The special geometry of kagome lattice leads to a wide range of interesting magnetic phenomena both in ferromagnets and anti-ferromagnets. In a ferromagnet, the flat band (localized mode) is observed at a finite energy level as seen in Figure 3-2.

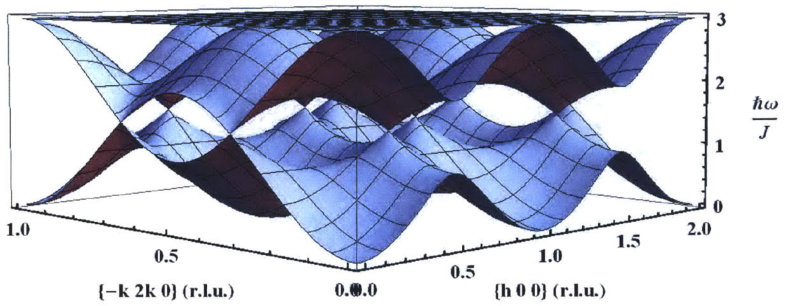

Figure 3-2: Localized band at finite energy level from [4].

This can be understood as follows. Consider Heisenberg spins on a ferromagnetic kagome lattice. The ground state is a simple collinear arrangement of all the spins facing the same direction (see Figure 3-3). Rather than having a large manifold of degenerate ground states, the kagome ferromagnet has a single ground state, up to a global spin rotation. This degeneracy of global rotation is also suppressed by the symmetry in crystals.

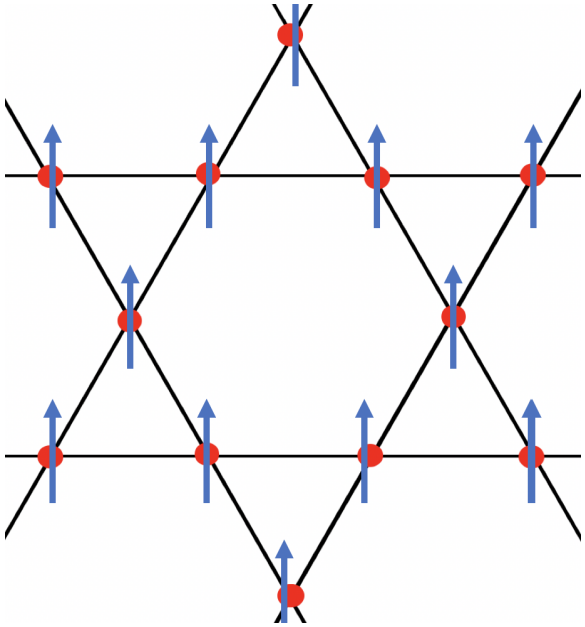

Figure 3-3: The ground state of a ferromagnet on the kagome lattice.

While the ground state has a rather simple appearance, the excited states are more

interesting. Figure 3-4 shows the localized excited states, where each of the six spins is rotated by 30 degrees so that the total change in angular momentum is equivalent to that of reversing one spin, with nearest-neighbor spins around the hexagon rotated in opposite directions.

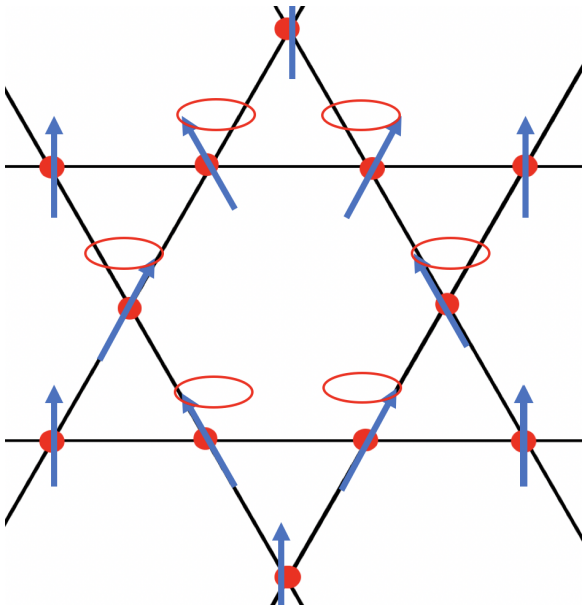

Figure 3-4: The excited localized state on the kagome lattice.

This excitation costs finite energy because the six bonds connecting these rotated spins as well as the twelve bonds connecting the rotating spins to their six unrotated nearest-neighbor spins. One can see these excitations in the momentum space in Figure 3-4, representing the flat band on the top of the dispersive bands. In real materials, different factors, such as the Dzyaloshinskii–Moriya (DM) interaction or the distortion from perfect kagome lattice, can easily distort this picture, leading to relaxation of the flatness of the band.

3.1.2 The Antiferromagnet Kagome Lattice

Geometric Frustration

Frustration in magnetism refers to a class of magnetic crystals where there exists no spin configuration that will satisfy all pairwise spin interactions simultaneously (in

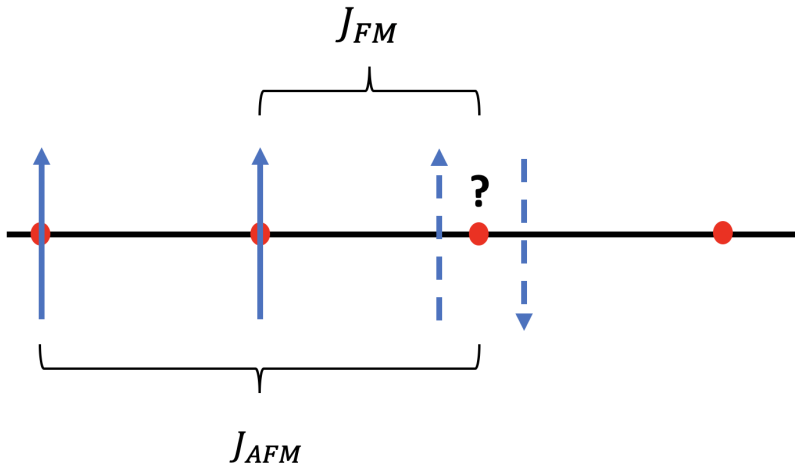

Figure 3-5: The 1-D Heisenberg chain.

which multiple configurations have the same energy) [17]. There are a number of possible sources of magnetic frustration. One of the simplest examples of frustration can be seen in the 1-D chain Heisenberg model [18] in Figure 3-5, where the nearest exchange interaction is ferromagnetic while the next-nearest interaction is antiferromagnetic. In this case, the competing interaction is the origin of the frustration. Frustration can also be a result of the disorder, as is the case in many spin-glass systems [19]. Geometric frustration refers to systems where the underlying geometry of the crystal lattice is the source of the frustration. In other words, geometrically frustrated materials are inherently frustrated, even in the absence of competing interactions or disorder.

To illustrate the concept of geometric frustration, let us first consider the non-frustrated case of antiferromagnetism on the square lattice, as shown in Figure 3-6. To clarify the difference between geometric frustration and the case of competing interactions, we assume that only the nearest interaction exists. Once the first spin (marked as 1) is placed, the nearest 2 and 3 are naturally determined to be the opposite sign of spins, resulting in the last node 4 having the same sign as the first spin. This logic applies to the other squares, which also meet the global energy minimum.

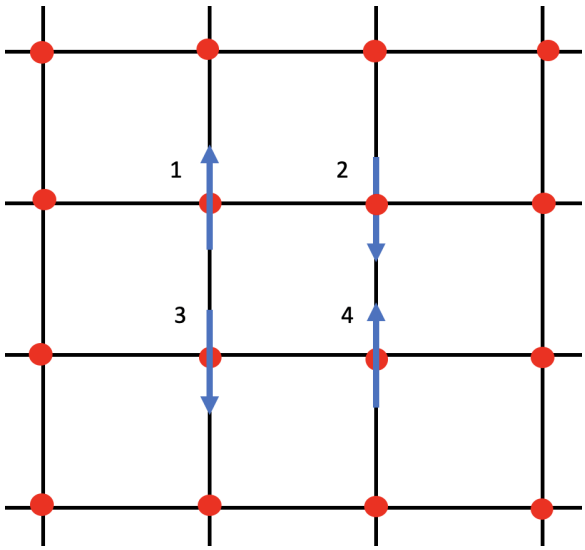

Figure 3-6: Antiferromagnetism on a square lattice.

In the case of the triangular lattice, on the other hand, spin configurations are not uniquely determined, as shown in Figure 3-7. Even though the other neighboring spins have the opposite sign compared to the first spin placed at 1, to meet the local energy minimum on 1-2 and 1-3 interactions, the other bond, 2-3 must have a higher energy combination. This cannot be resolved even if we start with different signs of spins in 2 and 3 and therefore no spin configuration can stabilize the system. This illustrates inherent geometric frustration, which is fundamentally different from the case of Figure 3-5, where the competition of the different interactions (the nearest and next-nearest interaction, in this case) is the source of the frustration.

In the above example, we implicitly assumed that spins can only point either up or down, that is the Ising model, but the Heisenberg model can relax the frustration. Figure 3-8 illustrates how the frustration of the Ising model is resolved in the Heisenberg model. All the spins have the exact 120° degrees rotation relative to each other: this configuration is not ideal locally since the opposite spins have the lowest exchange interaction but if we count all the exchange interaction in lattice the sum in the case of this 120°-degree configuration is smaller than that in Figure 3-7.

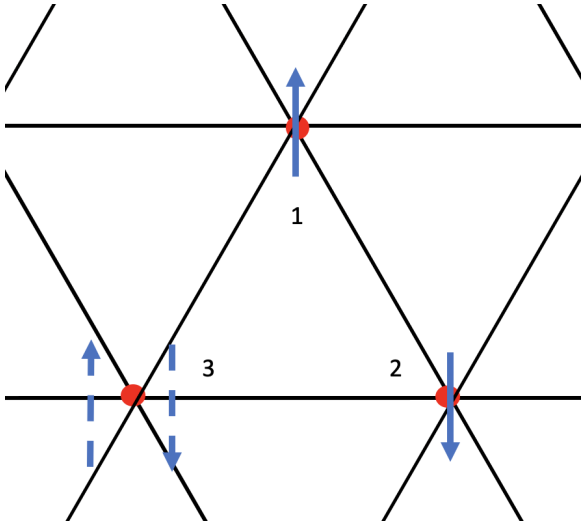

Figure 3-7: Antiferromagnet on triangular lattice: Ising model.

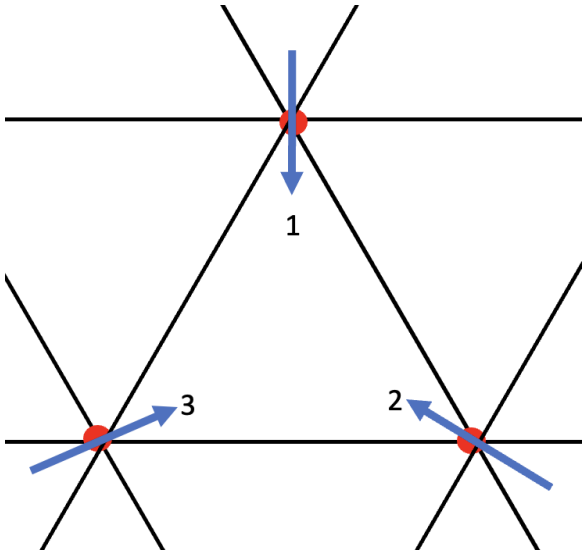

Figure 3-8: Antiferromagnet on triangular lattice: Heisenberg model.

Frustration in an anti-ferromagnet kagome system

The lesson from the previous section is the nearest neighbor antiferromagnetic system that has triangles is likely to be geometrically frustrated. The nearest neighbor antiferromagnet system on 2D kagome lattice, which consists of a triangular network of corner-sharing triangles, also has geometric frustration. Moreover, looking at the number of nodes connected to the node of the triangle, the kagome lattice has fewer nodes than that of the triangular lattice, which means more frustration energy is accumulated in each node. In terms of entropy per spin site in the Ising model, a kagome lattice has $0.502k_B$ [20], while a simple triangular lattice as shown in Figure 3-7 has $0.323k_B$ [21] at zero temperature.

To see how the structural difference between triangular and kagome structure affects the entire spin system, we focus on the neighboring two triangles as shown in Figure 3-9. In the Heisenberg scheme, the most energetically stable states in both triangles are the configurations where the neighbors share 120° degrees between them. Keeping this in mind, we consider fixing one spin (for example, 1). To lower the energy, the spins on 2, 3 and 4 in edge-sharing triangles are uniquely determined while spin 4 and 5 can still move around within the circle (marked as red in Figure 3-9) without changing the total energy. This arbitrary rotation of the two spins on the kagome lattice creates larger manifolds of ground states.

Weathervane mode in the kagome lattice

The large manifolds in the ground states of the kagome antiferromagnet in the Heisenberg model yield to the localized state which is also called the 'weathervane mode' [15]. This is the direct consequence of the arbitrary rotational freedom of the ground states (see Figure 3-9). If we constrain the spin configuration to be coplanar, all spins in the same triangle should point to any of the other two spin sites as shown in Figure 3-10. We can therefore describe the spin configuration in terms of three sublattices, one for each spin orientation. Consider a closed-loop or infinite open path formed by spins of our two chosen sublattices. We can rotate the spins along this loop, com-

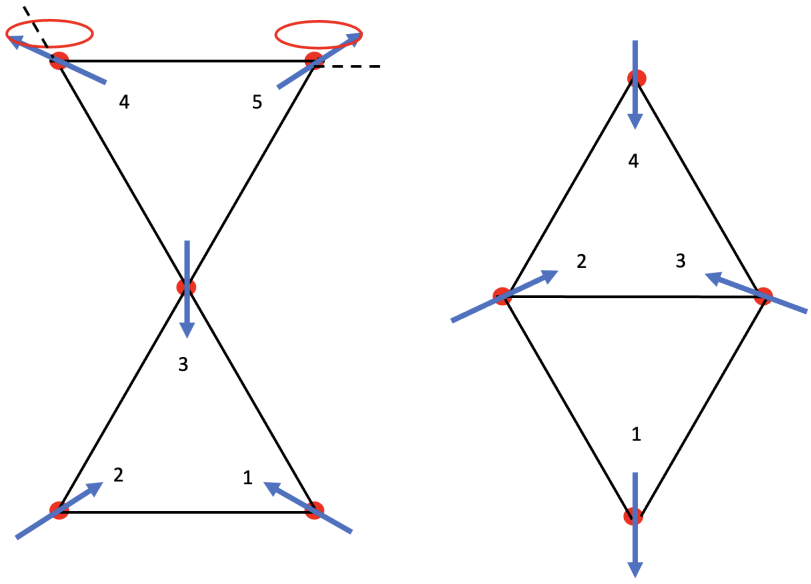

Figure 3-9: The corner-sharing triangles on kagome (left) and edge-sharing triangles on triangle lattice. In the case of edge-sharing triangles, once any spin (for instance 1) is fixed the other spins are uniquely determined. The corner-sharing triangles do not have this restriction: they still have other freedom of rotation of spins on 4 and 5 while keeping 120° degrees against their neighbors.

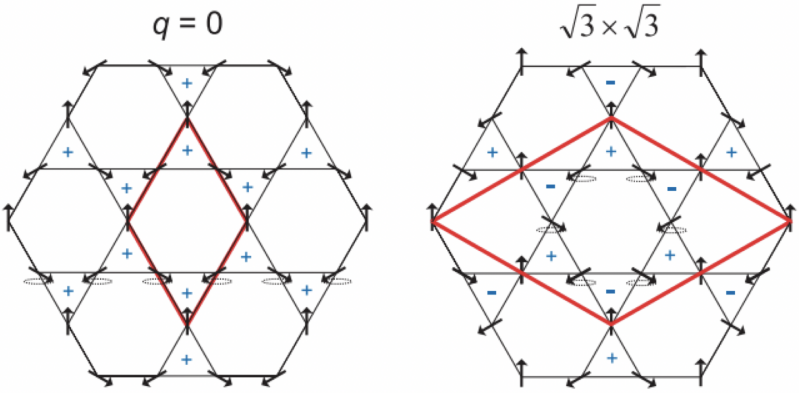

Figure 3-10: $q = 0$ spin configuration (left) and $\sqrt{3} \times \sqrt{3}$ (right). The plus and minus sign in each triangle stand for the chirality of spins as defined in the main text. The red rhombus is the unit cell of each spin configuration. From [5].

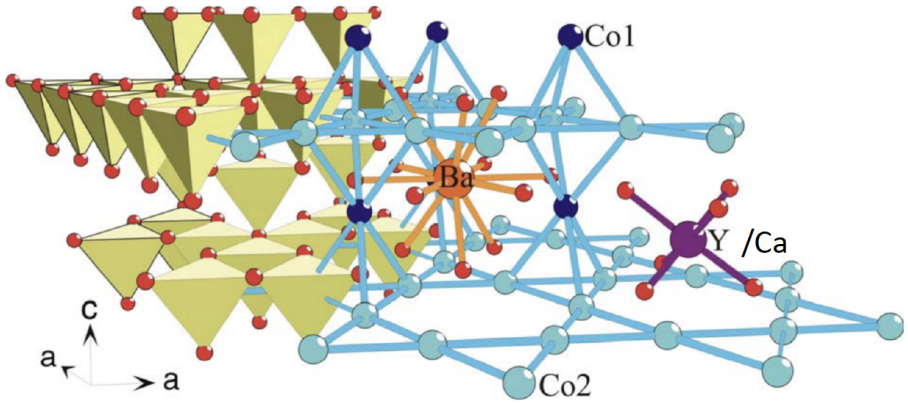

Figure 3-11: The crystal structure of $Y_{0.5}Ca_{0.5}BaCo_4O_7$ from [5].

pletely independent of the rest of the lattice. Because these modes are localized in real space they will be dispersionless in momentum space.

3.2 Magnonic flat band in $Y_{0.5}Ca_{0.5}BaCo_4O_7$

$Y_{0.5}Ca_{0.5}BaCo_4O_7$ is one of the candidates that may host the flat band from its structure shown in the Figure 3-11. One can see kagome layers consisting of Co sites (light blue atoms) and the spacer layers consisting of Y, Ca, Ba, and the other Co (dark blue atoms) between the neighboring kagome layers. According to a previous report [5], the dimensionality of the magnetic network of Co is 2-dimensional while another report [22] suggests that the Co in the spacer layer magnetically mediates an interaction between the kagome layers, creating a 3-dimensional network. According to inelastic neutron experiments [5], there is a flat band observed around the zero energy level (see Figure 3-12).

3.2.1 Magnetization Properties

As inferred from the geometry of Co atoms on the kagome layers, $Y_{0.5}Ca_{0.5}BaCo_4O_7$ has frustrated magnetism. The first report of magnetization of $Y_{0.5}Ca_{0.5}BaCo_4O_7$

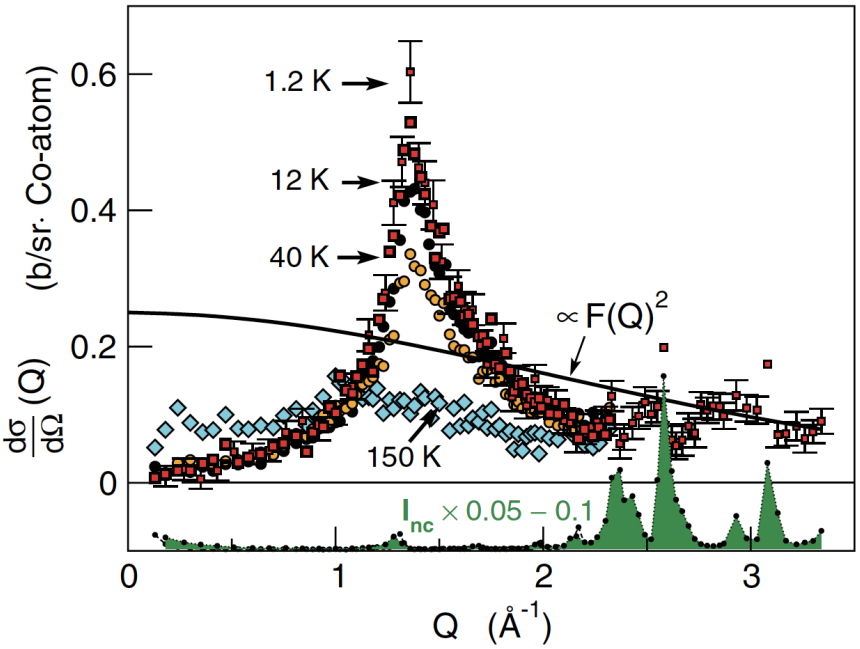

Figure 3-12: Spin-incoherent scattering of Co; the separated nuclear coherent scattering has been rescaled. From [5].

shows a multiple anomaly in the magnetization-temperature dependence and the Curie-Weiss temperature $\Theta_{CW} = -2200$ K [23], which indicates that the systems is very strongly frustrated system and its spin configuration in each temperature window is complex. Another report [5] suggests that a spin glass picture may be relevant given the discrepancy between field cooling and zero-field cooling.

Figure 3-14 shows the temperature dependence of magnetization of a single crystal of $Y_{0.5}Ca_{0.5}BaCo_4O_7$ grown by the floating zone method. Figure 3-15 shows the field dependence of the effective magnetic moment per Co atom. From these, we can see that remnant magnetization persists up to 400 K.

3.2.2 Electric Properties

As seen in the Figure 3-16, each compound is an insulator at all compostions $x = 0, 0.5$ and 1. The calculated band gap from $R = R_0 * e^{-\Delta/k_B T}$ is $\Delta_{Ca_{0.5}Y_{0.5}} = 52$ meV, $\Delta_Y = 440$ meV and $\Delta_{Ca} = 570$ meV, respectively. Figure 3-17 implies that the mean

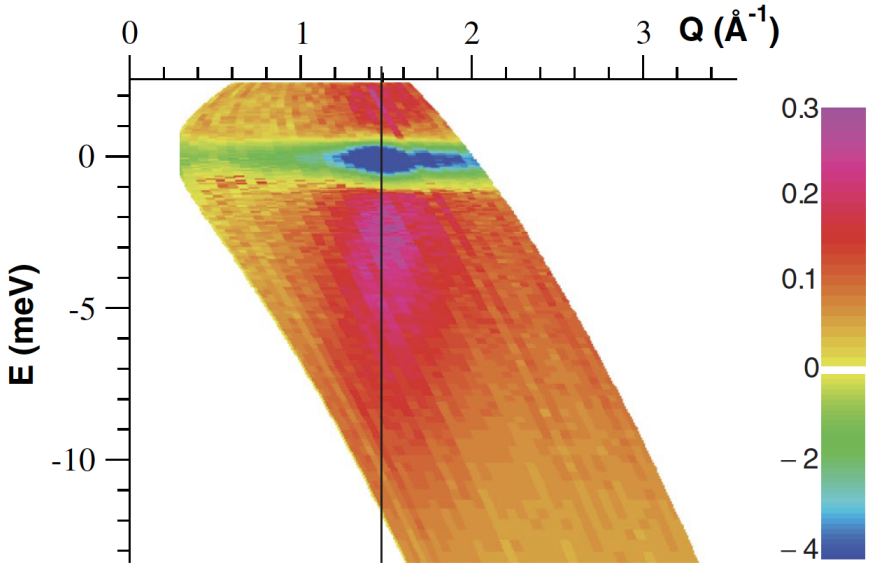

Figure 3-13: The difference of the intensity measured at 150 K and 40 K in time-of-flight mode reveals a loss of elastic signal (blue) and a relaxation one (red), which is consistent with the predicted flat band of the ground states of AFM kagome crystals. The quasi-elastic broadening at zero energy is considered to be from thermal spin fluctuations. From [5].

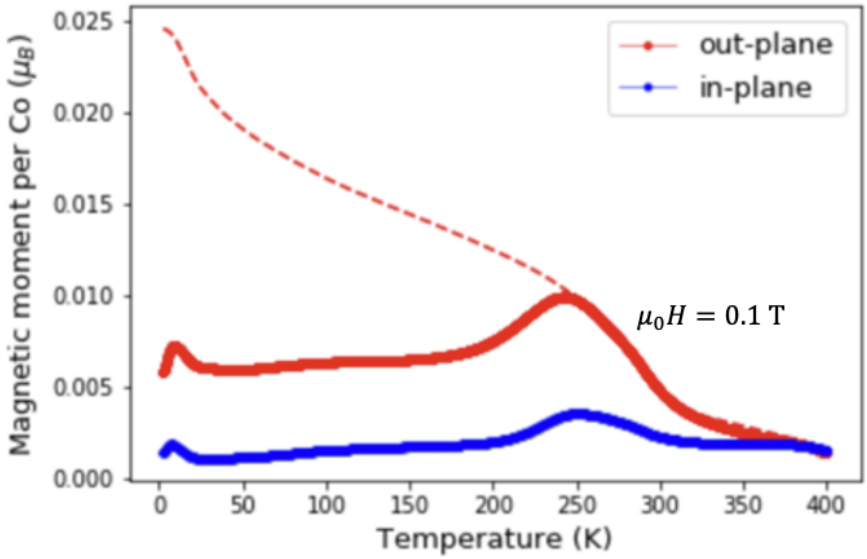

Figure 3-14: The effective magnetic moment per Co as a function of temperature for $Y_{0.5}Ca_{0.5}BaCo_4O_7$. The red line is measured with an out-plane magnetic field and the blue is with an in-plane field. Zero-field cooling measurement is dotted line while field cooling is the solid line. From [5].

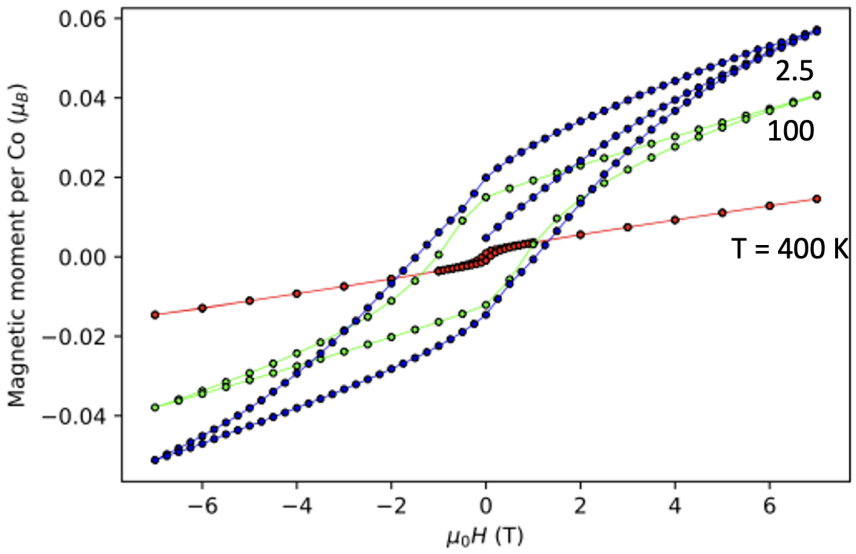

Figure 3-15: Magnetic field dependence of magnetization of $Y_{0.5}Ca_{0.5}BaCo_4O_7$ at selected temperatures

free path of charged carriers is very short since the change of magnetoresistance (MR) is very small at all temperatures. The hysteresis observed below 100 K suggests the magnetic property also has hysteresis behavior, such as spin glass or ferromagnetic. In this case, the hysteresis of spin-glass behavior also causes the butterfly-like shape in magnetoresistance.

3.2.3 Anomalous Hall coefficient

Figure 3-19 shows that the coercive field in the Hall resistivity in the Figure 3-18 is related to that of magnetization-temperature dependence in Figure 3-14. The hall component can be extracted by the following [24]:

$$\rho_{yx}(\mu_0 H) = \rho_0 + \rho^{AHE}, \tag{3.1}$$

$$\rho^{AHE} = \mu_0 M R_s, \tag{3.2}$$

$$R_s = \rho^{\beta} \tag{3.3}$$

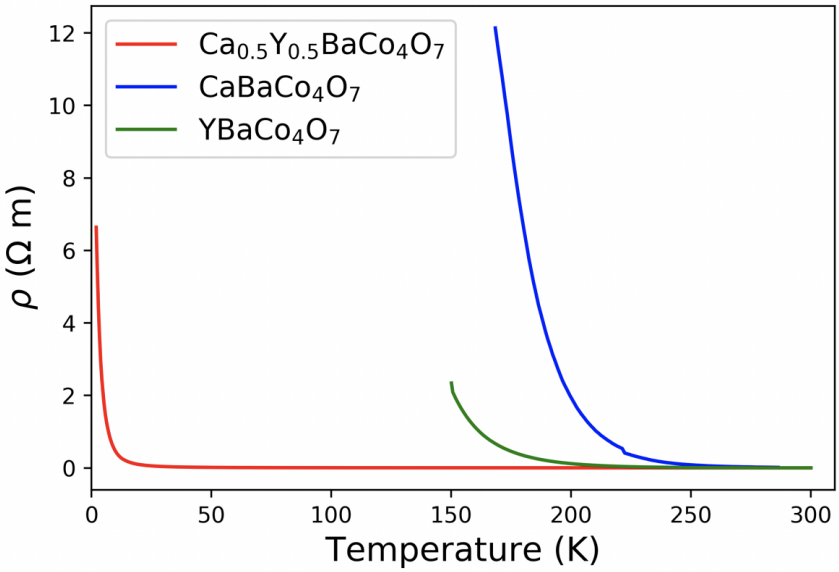

Figure 3-16: Temperature dependence of resistivity of each compound. The extracted band gaps are $\Delta_{Ca_{0.5}Y_{0.5}} = 52$ meV, $\Delta_Y = 440$ meV and $\Delta_{Ca} = 570$ meV.

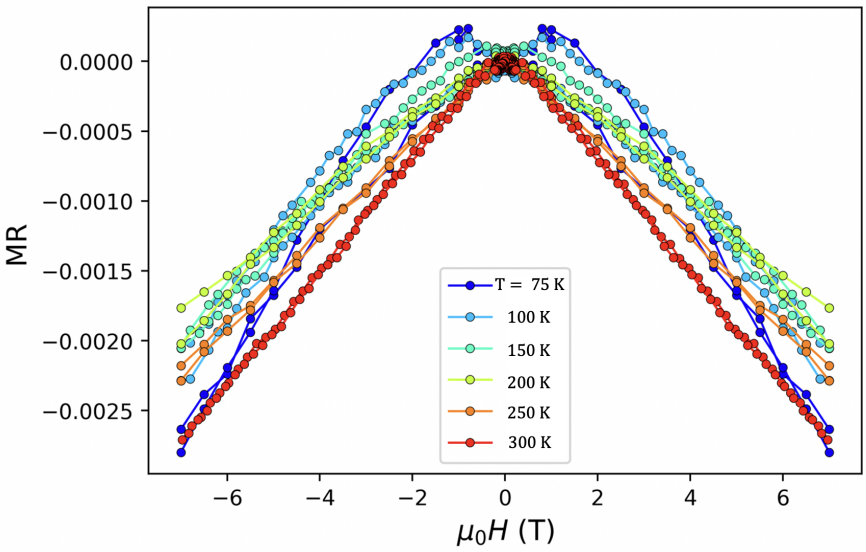

Figure 3-17: Magnetoresisitance of $Y_{0.5}Ca_{0.5}BaCo_4O_7$ at different temperatures. The change is lower than 1 percent at all temperatures.

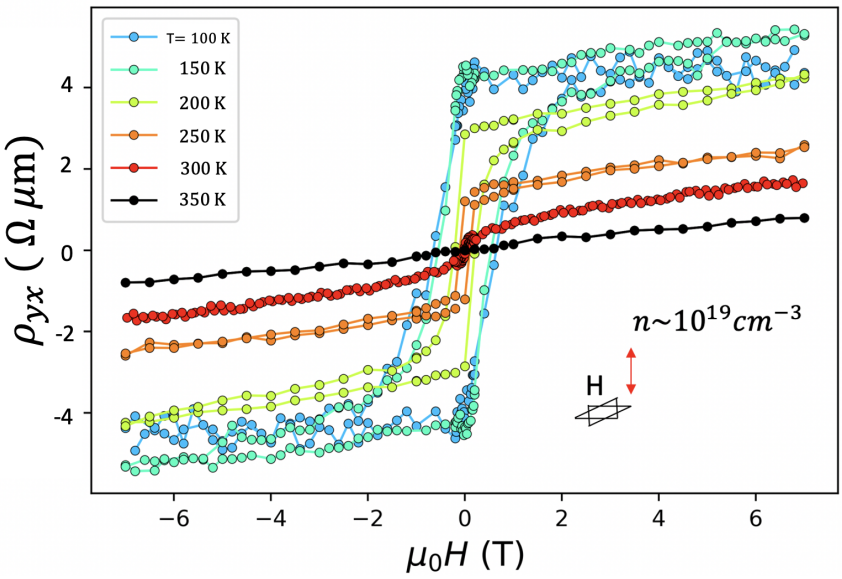

Figure 3-18: The Hall resistivity of $Y_{0.5}Ca_{0.5}BaCo_4O_7$ from 350 K to 100 K. The carrier density is calculated from the slope where the strength of the field larger than 2 T.

where ρ_0 is the normal Hall term, that is the linear part as a function of the field at a higher magnetic region ($>$ 2 T). The anomalous component is extracted by the intersection between the y-axis and the normal Hall term extrapolated from the higher field. Furthermore, as suggested in [24], ρ^{AHE} is characterized by its resistivity corresponding to its underlying Hall mechanism. The side jump, where the electron is deflected in the opposite directions by the opposite electric fields experienced on approaching and leaving and impurity, is characterized by $\beta = 2$, while the skew scattering, caused by the spin-orbit coupling between electron and impurity, is $\beta = 1$. In the case of $Y_{0.5}Ca_{0.5}BaCo_4O_7$, as illustrated in the Figure 3-20, the side jump mechanism is corresponding the temperature window between 200 K and 300 K.

3.3 Thermal properties of $Y_{0.5}Ca_{0.5}BaCo_4O_7$

The thermal properties of $Y_{0.5}Ca_{0.5}BaCo_4O_7$ is investigated here in single crystal specimens.

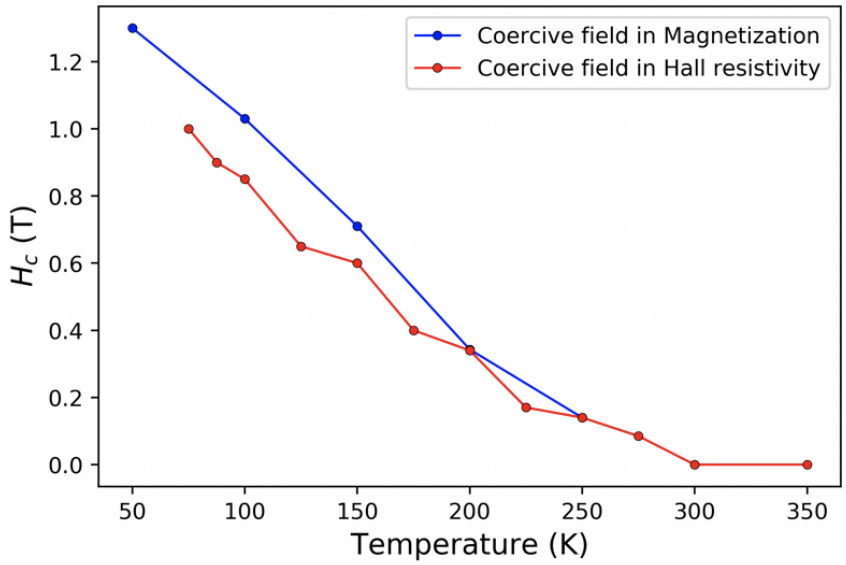

Figure 3-19: The coercive field of $Y_{0.5}Ca_{0.5}BaCo_4O_7$. The coercive field is estimated as the x-coordinate of the intersection of the x-axis and each measurement curve.

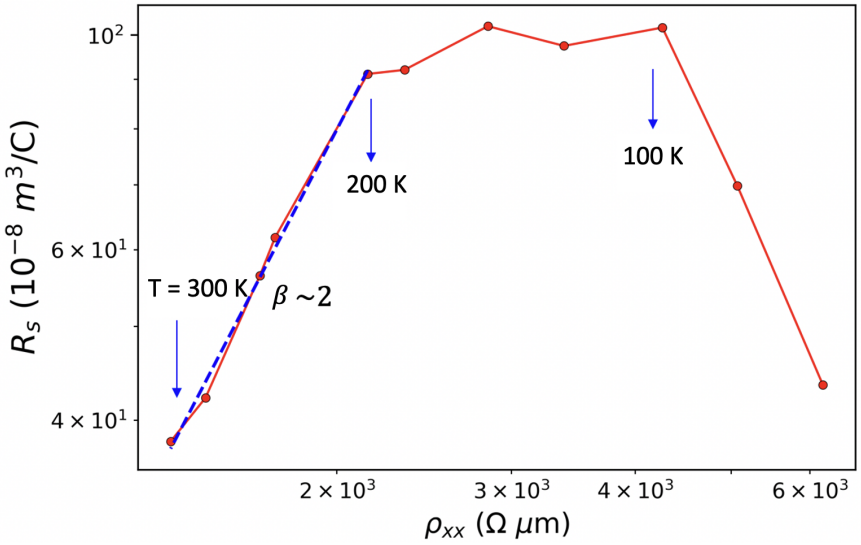

Figure 3-20: Anomalous coefficient R_s as a function of ρ for $Y_{0.5}Ca_{0.5}BaCo_4O_7$. R_s is calculated by Eq. (3.1).

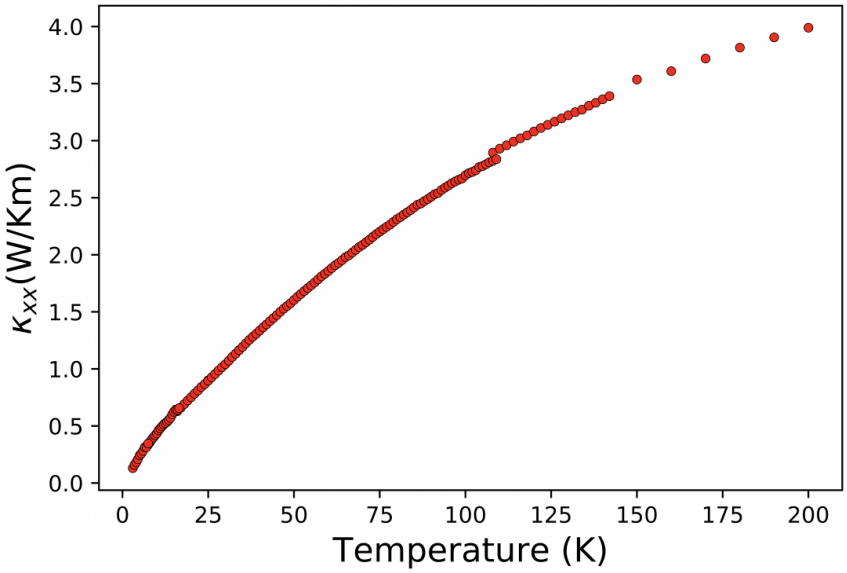

Figure 3-21: Thermal conductivity of $Y_{0.5}Ca_{0.5}BaCo_4O_7$ from 200 K to 7 K.

3.3.1 Thermal conductivity

Figure 3-21 shows the thermal conductivity from 200 K to 7 K. Throughout the temperature window, there is no anomaly other than measurement errors around 100 K and 20 K due to the change of the power of the heater. The insensitivity against the applied magnetic field in Figure 3-23 indicate that no conventional heat transport originated from the magnetism exists. In particular, the weathervane mode is not observed in $Y_{0.5}Ca_{0.5}BaCo_4O_7$. Moreover, the scaling at low-temperature as shown in Figure 3-22 indicates a complex phonon mechanism.

3.3.2 Heat Capacity

The temperature dependence of heat capacity in Figure 3-24 also has no anomaly at the temperature range between 230 K to 7 K. The characterization by temperature suggests a 3-dimensional phonon excitation. From this, we conclude that no signatures of the flat band is observed in $Y_{0.5}Ca_{0.5}BaCo_4O_7$.

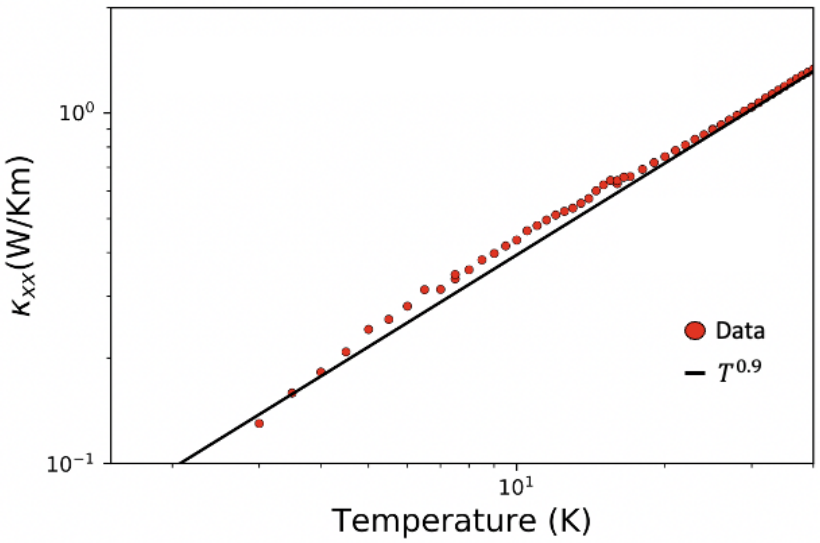

Figure 3-22: Scaling of $\kappa_{xx}t$ by T^{β} for $Y_{0.5}Ca_{0.5}BaCo_4O_7Y_{0.5}Ca_{0.5}BaCo_4O_7$. $\beta \approx 1$ indicates that, unlike $\beta = 3$ for a typical insulator, complex phonon scattering controls the thermal conduction at low temperature.

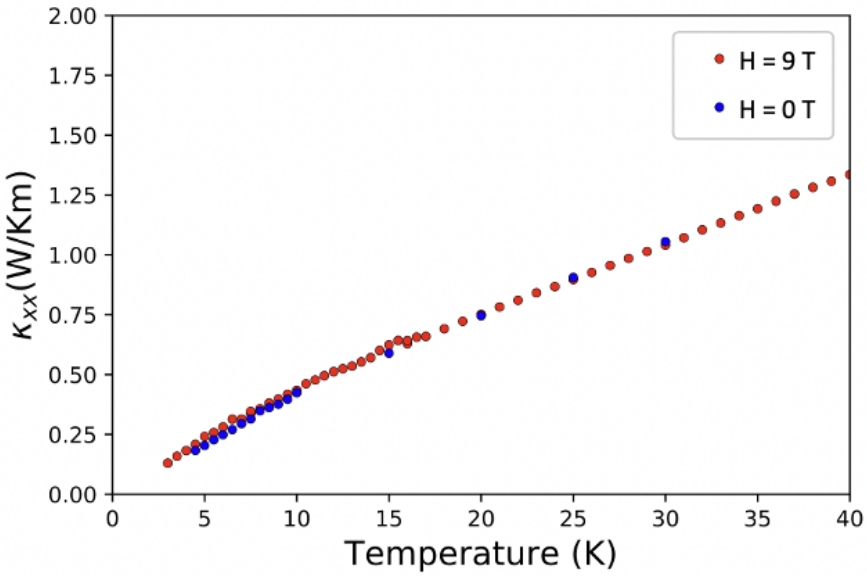

Figure 3-23: The field dependence of thermal conductivity of $Y_{0.5}Ca_{0.5}BaCo_4O_7$.

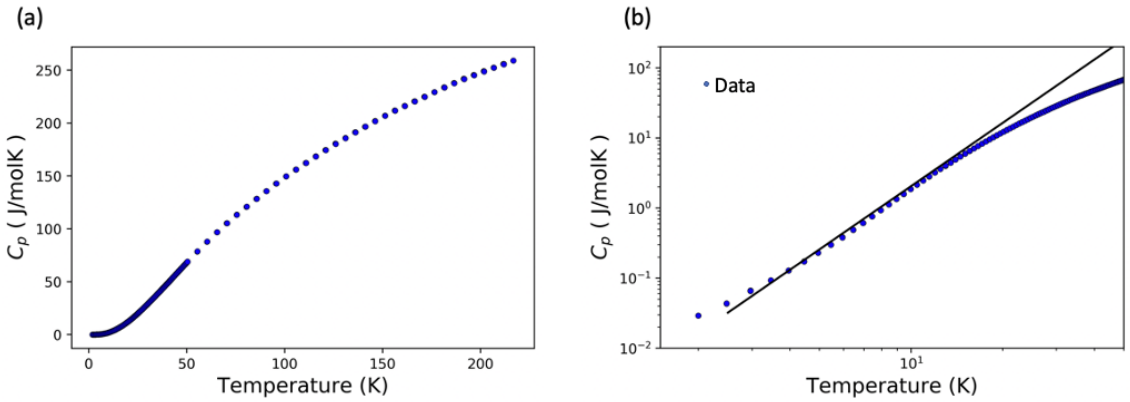

Figure 3-24: (a) Heat capacity of $Y_{0.5}Ca_{0.5}BaCo_4O_7$ as function of temperature from 5 to 200 K. (b) The scaling by T at low temperature, T^3, indicates an absence of a conventional magnetic band contribute to the heat capacity.

3.3.3 Summary

We showed the experimental approach to test if the series of the compounds, $Y_xCa_{(1-x)}BaCo_4O_7$, have an exotic thermal transport originated from magnon flat band. $Y_{0.5}Ca_{0.5}BaCo_4O_7$ has a flat magnonic band at zero energy level as observed by the inelastic neutron scattering [22]. This flat band is considered to be generated by the geometric frustration on kagome layers where Co ions antiferromagnetically interact with each other. In our transport and specific heat measurements, however, we do not observe any signatures of the flat band. The anomalous Hall effect, instead, is observed in electrical transport experiments. By comparing the temperature dependence of magnetization with that of the Hall transport as seen in Figure 3-19, we can infer that the observed AHE is correlated to the magnetization, possibly to the spin configuration on the kagome layer. More advanced experiments such as neutron scattering are needed to confirm the spin texture at each temperature range to discuss the relation between the AHE and the intrinsic magnetization on the kagome layer.

Chapter 4

Material Informatics

4.1 Introduction

4.1.1 Advent of data-driven materials discovery

Innovations in materials have brought productivity and prosperity to society. In turn, modern technology relies on the discovery of new materials. However, the creation and development of novel materials with desired properties is a difficult and slow process. This is because a large part of the material discovery process is still driven by experimental trial and error; in fact, many milestone materials were discovered by accident rather than careful strategy. For example, the growth method of the blue LED host, GaN film, was accidentally discovered by using a mulfunctional furnace [25]. The first high temperature superconductor, the copper oxide superconductor, was not expected and remains a challenge to model as it cannot be explained by the conventional BCS theory [26].

The history of the computational approach for material exploration started with the development of quantum mechanics in the early 20th century. Solid-state physics shifted the paradigm to use physical laws and semi-empirical models to guide the design of new materials. Up to today, exploring neighboring elements in the periodic table is still one of the most efficient ways to achieve target physical properties. In the late 20th century, increasingly powerful computers began to allow the direct

computing of material properties by solving the Schrödinger equation. The success of *ab-initio* simulations, especially density functional theory [27], motivated the computational exploration of the vast data of materials.

Many expect that data-driven approaches including machine learning will lead to a new paradigm for materials discovery [28]. This trend was brought about partly by the remarkable improvement of computation power and also by the advent of large-scale open data sources. For example, a recent review paper summarized 10 computational databases and 11 experimental databases that are publicly accessible [28]. These open databases provide a new guideline for materials synthesis by utilizing a large number of datasets.

Computational material exploration especially in materials such as inorganic crystals and molecular substances is called materials informatics. Recently, in materials informatics more researchers are trying to incorporate a large amount of datasets into first principle calculation or machine learning models to predict materials properties. Following the rapid advance of deep learning methods used in image recognition, and natural language processing, many deep learning techniques have been applied to materials systems [29, 30]. Even though these new generations of computational approach can potentially capture the features of materials which cannot be caught by the classical approaches and realize better performance, the range of target properties is still limited. One of the reasons many deep learning models can only predict limited physical properties is that an open database of materials [31] cannot provide sufficient examples and often they are calculated rather than experimental values. In this chapter, I study classical and modern deep machine learning models to predict magnetic properties with experimental data.

4.1.2 Classical machine learning

Before going to the machine learning architecture, it is helpful to introduce the broader concepts of machine learning. The concept of machine learning is usually defined as the schematic in Figure 4-1 [32].

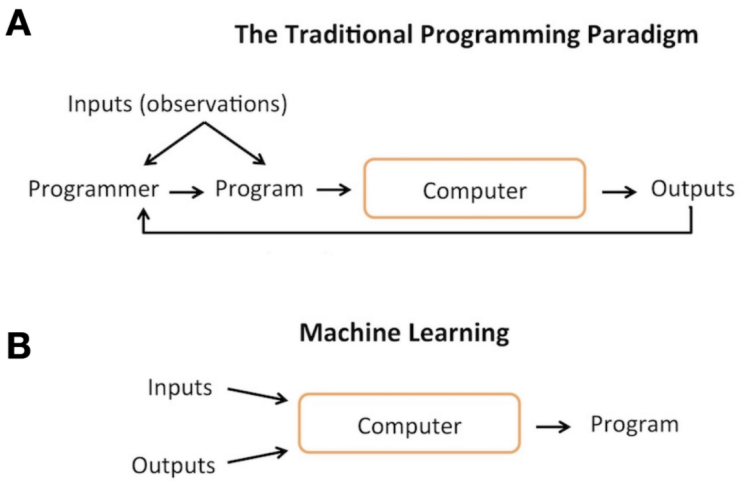

Figure 4-1: Comparison between traditional programming (A) and machine learning (B). The schematic is from [6].

The type A flowchart in Figure 4-1 describes the traditional programming paradigm where a programmer develops a set of rules, feeds it to the computer and observes the output. If the outputs are not satisfactory, the programmer goes back to the program and adjusts the rules to improve the results. Therefore, the action of modification is done by humans.

Unlike the traditional programming paradigm, machine learning is usually referred to as the process of letting the computer discern such non-trivial input-output relationships. As summarized in the type B flowchart in the 4-1, the difference between the traditional programming paradigm and machine learning is that the latter is a computer algorithm with the task we want to solve, and it will generate the decision-making program that optimizes the decision making.

4.1.3 Deep learning

The first deep machine learning algorithms appeared in the 1950s and were designed to mimic the networks of neurons in the human brain [7] as seen in Figure 4-2. In the following decades, neural networks with multiple neurons and layers were developed

as well as algorithms to train them effectively.

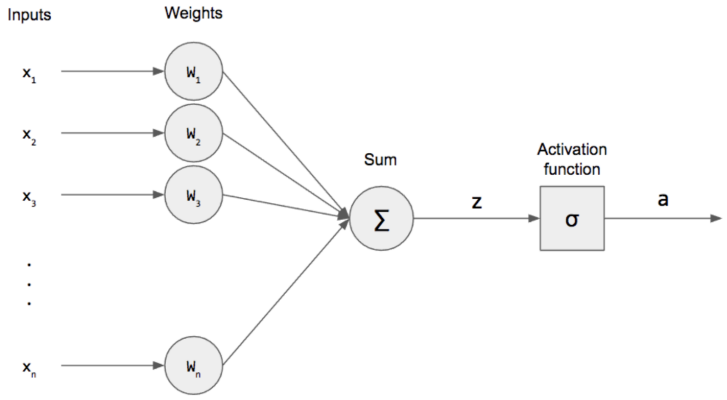

Figure 4-2: Flowchart of perceptron. From [7].

Due to the rapid development of deep learning methods recently, as well as improvement of calculation power, the branch of machine learning that does not concern deep neural networks is now referred to as conventional machine learning. The relation between deep learning and machine learning is represented in Figure 4-3.

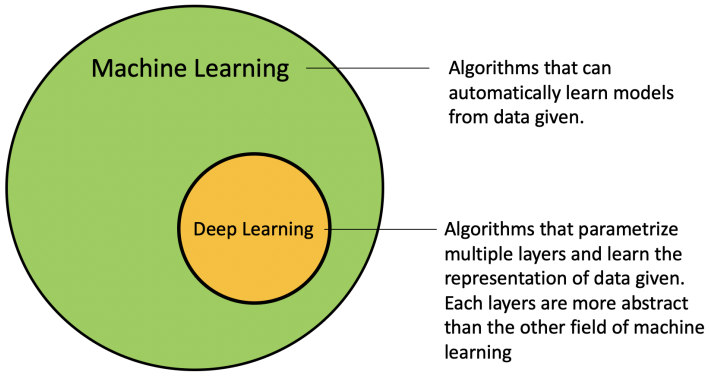

Figure 4-3: The overlap between machine learning and deep learning.

4.2 Data driven materials exploration of new magnets

Magnetism in crystals is generally understood by two different pictures: one is by the spin localized picture where the local spins tied to the magnetic nodes interacting with each other yield macroscopic magnetism, while the other is by band structures where the intrinsic magnetization lowers the band energy. In this study, we are interested in the former cases because local spin-based magnetic compounds tend to show a high structure-properties correlation and will be compatible with large data-driven machine learning architecture for the following reasons.

1. The data quality other than structure data such as bandgap, formation energy, and other physical properties is less reliable.

2. There are many structure data such as cif data files available in many open databases (*e.g.* [31]).

3. Some magnetic properties such as magnetic order (anti-ferromagnet or ferromagnet) are strongly related to its structure and chemical information.

In this work, among the variety of magnetic properties, we will focus on two: the type of magnetic order and the critical temperature. The type of magnetic order usually consists of three types: ferromagnetic, where the atomic spins align along the same direction, anti-ferromagnetic, where the atomic spins lower their energy most by aligning antiparallel, and paramagnetic. A magnetic order disappears above a certain temperature, and that is known as the critical temperature T_C; these are the Curie temperature in the case of ferromagnets and the Neel temperatures in the case of anti-ferromagnets.

4.3 Crystal Graphical Convolutional Neural Networks

To extract critical information effectively from the original structural information of crystals (*e.g.* cif format), we use the Crystal Graphical Convolutional Neural Networks (CGCNN), which was originally suggested by Xien Tian [8], to create a graphi-

cal representation based on the atomic sites and bond length between them. The core idea of CGCNN is illustrated in the Figure 4-4 ([8]): a crystal graph G is an undirected graph that allows multiple edges between the same pairs to reflect the periodicity of the crystals. Each node is denoted by a vector v_i which is designed to represent the atomic features in the periodic table. In the same way, an edge between the site i and j is represented by a feature vector $u_{(i,j)k}$, where k is the k-th bond connecting i and j.

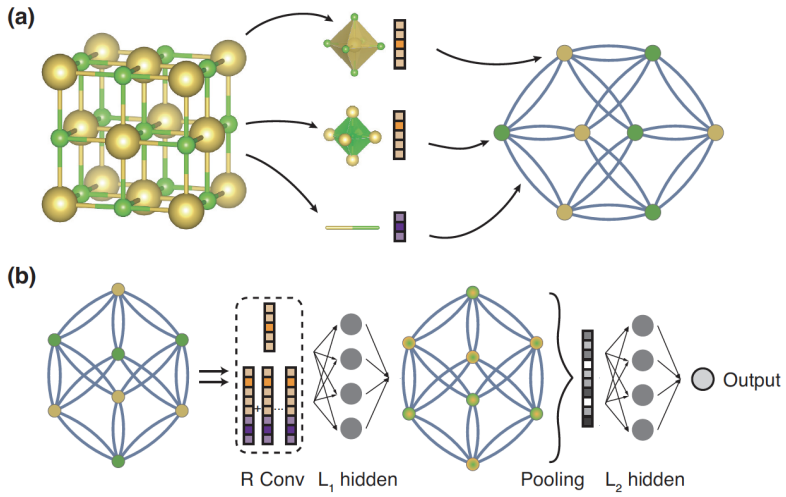

Figure 4-4: Graphical representation of crystal structure in the CGCNN. (a) Nodes and edges in the graph are represented by vectors corresponding to the atomic sites and bonds, respectively. (b) The architecture of the CGCNN on the top of the crystal graph. R convolutional layers and L_1 hidden layers create a new graph with each node representing the local environment of each atom. After being pooled, the new graph is connected to L_2 hidden layers and then to the output layer. Figure adapted from [8].

To encode the similarity/difference of different elements in a node feature vector, the atomic properties in Table 4.1 are selected for each component of the initialized vector. This enables CGCNN to distinguish different atoms.

Property	Unit	Range	# of categories
Group number	–	1,2, ..., 18	18
Period number	–	1,2, ...,	9
Electronegativity	–	0.5–4.0	10
Covalent radius	pm	25–250	10
Valence electrons	–	1, 2, ..., 12	12
First ionization energy	eV	1.3–3.3	10
Electron affinity	eV	-3–3.7	10
Block	–	s, p, d, f	4
Atomic volume (Log)	cm^3/mol	1.5–4.3	10

Table 4.1: Tables of properties used in the node feature vectors

The original CGCNN paper proposes two possible methods to define the connectivity of the edge $u^k_{(i,j)}$. The first only considers the strong bonding interaction while the second method tracks the nearest neighbors in the original structure. Throughout this work, we use the second method to define the connected nodes. After the connectivity is defined, the edges are defined from the distance between them as,

$$u^{ini}_{(i,j)} = exp(-(d(i,j) - \mu)^2/\sigma^2) \tag{4.1}$$

where $\mu = 0.2$ and $\sigma = 0.2$.

4.4 Design of Magnetic Graph Representation

As illustrated in the previous section, the application of the CGCNN itself is very general. We consider here modifying the original crystal graph representation into the magnetic graph representation. The magnetic graph is the specific graph representation where the non-magnetic atoms are removed and only magnetic atoms exist so that we enable the CGCNN to make better predictions on spin localized magnetic systems. The definition of the nodes of the magnetic graph is the same as the original CGCNN. The edge of the magnetic graph should reflect the strong magnetic interaction between different magnetic sites. One of the examples of the edges is the exchange interaction in the Heisenberg model. In this work, we use the bond length

as the edges of the magnetic graph.

4.5 Performance of Magnetic CGCNN

To test the performance of the magnetic CGCNN, we use the experimental properties scraped from published papers. The scraping method used in this work was previously reported [33]; it collects the critical temperature of ferromagnets and antiferromagnets from 50 journal articles. The profile of the collected data is shown in Figure 4-5. There are two rules used in this work to cleanse the original dataset. (1) The chemical formula should have an integer form (ones that have fractional stoichiometric values have been removed) and (2) the compound should have magnetic atoms (ions).

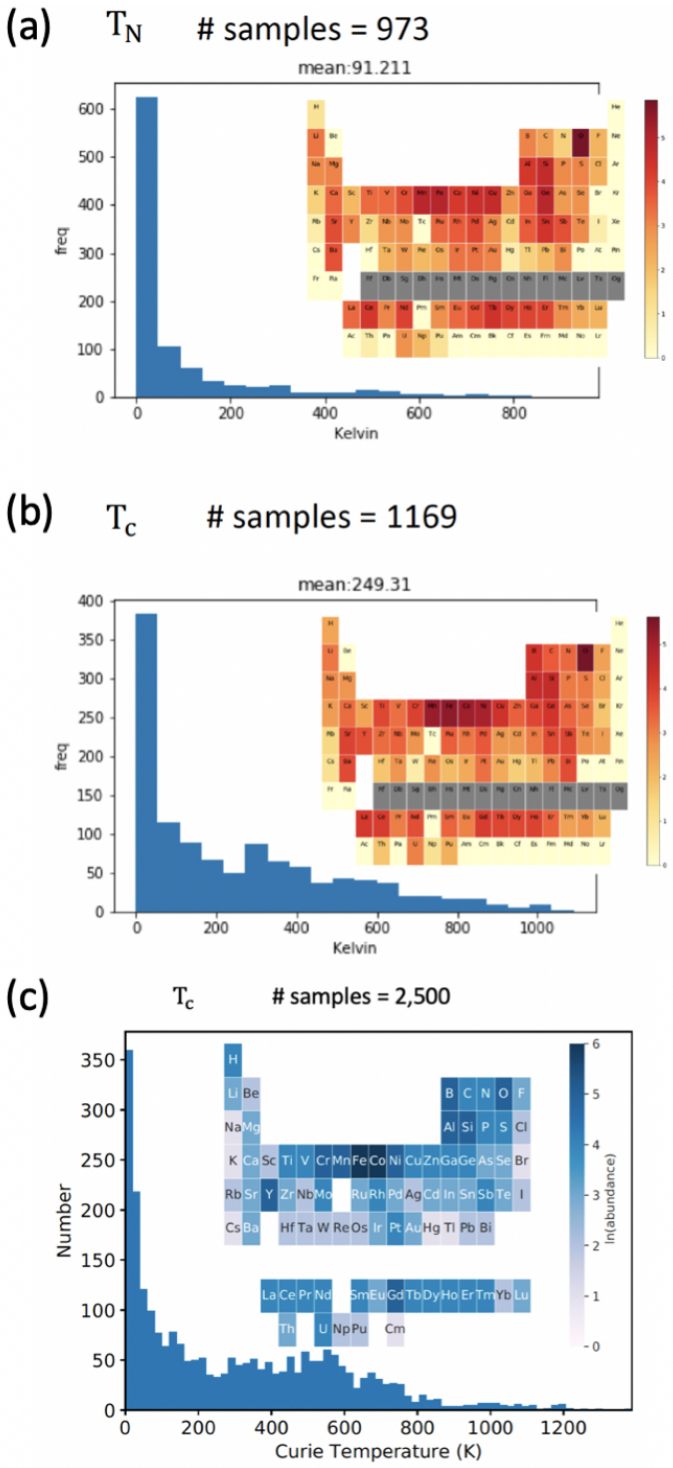

Figure 4-5: The profile of the dataset (a) The dataset of Neel temperature. (b) The dataset of Curie temperature. (c) The dataset used in the literature [9].

After these cleansing processes, the remaing dataset of each magnetic type is 973 anti-ferromagnets and 1169 ferromagnets. The database used in this work generally has atoms across the entire periodic table. Several tendencies are observed: more compounds have the transition metals than other magnetic atoms and many compounds are oxides (284 out of 1169). This implies the dataset can be a good training set because magnetism of transition metal compounds and oxides are usually understood as the spin localized picture, thus, within the range of the magnetic CGCNN.

Figure 4-6 is the performance of the regression predictions in each model. Figure (a) in 4-6 is the conventional random forest regression with the typical structural and elemental features listed in Table 4.2, showing the best performance. Figure 4.2 (b) and (c) are the CGCNN with original and magnetic graph representation, respectively. The CGCNN with the magnetic graph has smaller Mean Absolute Error (MAE) and loss for the test dataset than the original CGCNN.

Features	Symbol	Dim.
L^p stoichiometry norm ($p = 1, 2, 3$)	$\|\|x\|\|_p$	3
Stoichiometry entropy	S	1
Atomic fraction vector	$\mathbf{v}_{\text{chem}}$	84
CW atomic number	$\langle Z \rangle$, $\langle \|Z\| \rangle$, $\langle \Delta Z \rangle$	3
CW valence electrons	$\langle N_{\text{V}} \rangle$, $\langle \|N_{\text{V}}\| \rangle$, $\langle \Delta N_{\text{V}} \rangle$	3
CW period	$\langle P \rangle$, $\langle \|P\| \rangle$, $\langle \Delta P \rangle$	3
CW group	$\langle G \rangle$, $\langle \|G\| \rangle$, $\langle \Delta G \rangle$	3
CW molar volume	$\langle V \rangle$, $\langle \|V\| \rangle$, $\langle \Delta V \rangle$	3
CW melting T	$\langle T_{\text{M}} \rangle$, $\langle \|T_{\text{M}}\| \rangle$, $\langle \Delta T_{\text{M}} \rangle$	3
CW electronegativity	$\langle \epsilon \rangle$, $\langle \|\epsilon\| \rangle$, $\langle \Delta \epsilon \rangle$	3

Table 4.2: The feature vector used in the literature [9]. The total dimension of the vector is 129, each component of which is uniquely determined once the chemical formula is given.

Figure 4-7 shows the classification of anti-ferromagnets and ferromagnets in each CGCNN model. As well as the regression of T_C, the CGCNN with magnetic graph shows a better result than the original CGCNN.

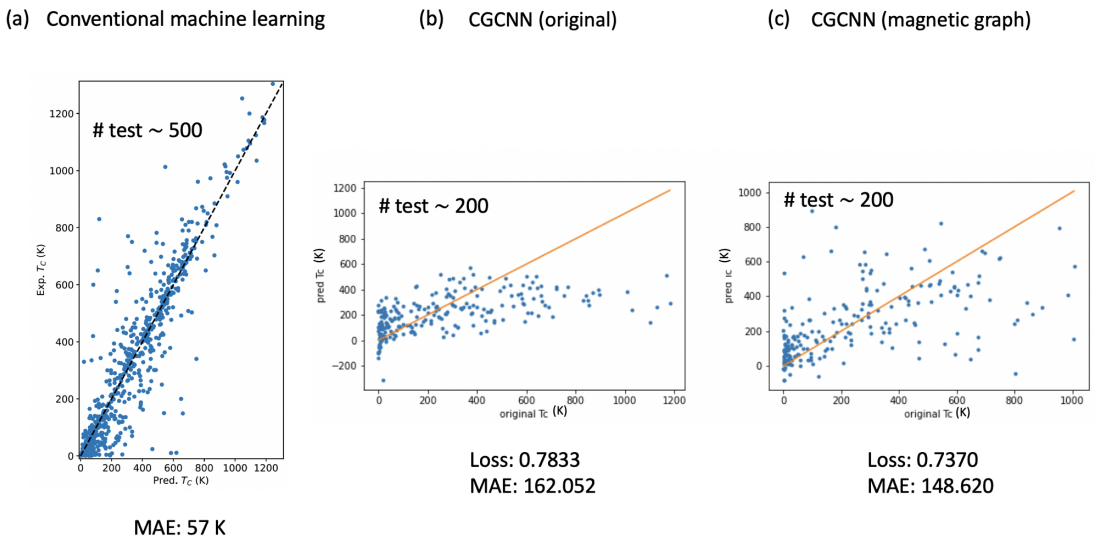

Figure 4-6: The predicted T_C for the test dataset in each regressor: (a) random forests with features vector listed in 4.2 (b) The original CGCNN (c) The modified CGCNN with the magnetic graph representation.

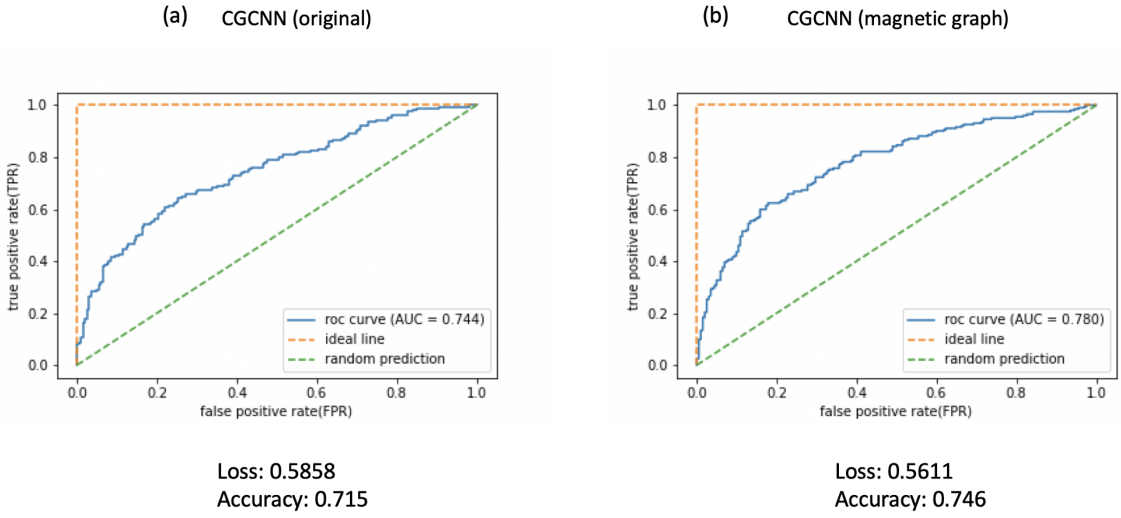

Figure 4-7: The ROC (Receiver operating characteristic) curve for the classification of ferromagnets and anti-ferromagnets for (a) conventional CGCNN and (b) magnetic CGCNN.

Overall, even though the CGCNN does not outperform the conventional machine learning approach, the magnetic graph representation slightly improves the performance of the CGCNN both in regression and classification, indicating that the idea of removing non-magnetic atoms in graph representation is effective. In the context of the spin localized picture, these results imply that the structure of magnetic sites is more influential to the macroscopic magnetism than that of non-magnetic ones.

4.6 Future directions

Uncorrelated input data in training datasets often reduce a model's performance. In the case of this study, there are metallic magnets and insulating magnets included in the same dataset, which possibly affects the model as the underlying mechanism of magnetism is different for the two. For instance, the ferromagnetism of elemental Fe is understood by the band structure near Fermi energy rather than localized spin models. Furthermore the element of the magnetic ion itself is strongly correlated to magnetism. For example, compounds which have the Mn elements as the magnetic ions are more likely to be anti-ferromagnet compared to the ones with elemental Fe.

One of the possible ways to resolve this issue is to use a filter for preprocessing. For example, by separating insulators from metals or Mn-included compounds from Fe-included ones, the model can learn the features within each category without being disturbed by uncorrelated samples. Another possible way is to use the technique of attention in a model. The Graph convolutional neural networks with global attention (CrabNet) [34] is one of the CGCNN models which introduce an attention mechanism to distinguish the compositional difference, which could help the predictive performance of magnetic properties.

Finally, of great interest is the future appreciation of these methods to discover new frustrated magnetic systems that may be explored experimentally for flat band related phenomena.

Chapter 5

Summary and Outlook

In summary, we showed the experimental approach to test if a series of the compounds, $Y_xCa_{(1-x)}BaCo_4O_7$, have an exotic thermal transport originated from a magnon flat band. Among this family, $Y_{0.5}Ca_{0.5}BaCo_4O_7$ has a flat magnonic band at zero energy level as observed by inelastic neutron scattering [22]. This flat band is considered to be generated by the geometric frustration on kagome layers where Co ions antiferromagnetically interact with each other. In our transport and specific heat measurements, however, we do not observe any signatures of the flat band. The anomalous Hall effect, instead, is observed in electrical transport experiments. By comparing the temperature dependence of magnetization with that of the Hall transport as seen in Figure 3-19, we can infer that the observed AHE is correlated to the magnetization, possibly arising from the spin configuration on the kagome layer. More advanced experiments such as neutron scattering are needed to confirm the spin texture at each temperature range to discuss the relation between the AHE and the intrinsic magnetization on the kagome layer.

The above approach to find the magnetic compound with the flat band is based on the following observations. Firstly, the magnetic ions (Co) form a kagome network which is expected to host a weathervane mode as discussed in chapter 3. Secondly, the Curie-Weiss temperature is very high (over 1000 K), could lead to large magnon thermal transport. Another factor is the growth method of the single crystal is feasible in our laboratory. These considerations can be dealt with more systematically,

motivating the data-driven materials discovery approach. The CGCNN deep learning model was applied to magnetic systems, in particular, to make the regression model of the transition temperatures and the classification (ferromagnetic or antiferromagnetic) model. Magnetic CGCNN is the model which only focuses on the magnetic ions with removing non-magnetic ions from original structures. In the classification prediction, the magnetic CGCNN has better accuracy than that of the CGCNN, which indicates that the magnetic properties could be predicted only from the structure of the magnetic ions. Within the framework of this thesis, I only consider a very broad category of the magnetic properties but, in future work, more granularized material properties (for instance, magnon thermal conduction, magnetic frusration, or topological magnetic compounds) could be the target of the prediction.

Bibliography

[1] M. Asen-Palmer, K. Bartkowski, E. Gmelin, M. Cardona, A. P. Zhernov, A. V. Inyushkin, A. Taldenkov, V. I. Ozhogin, K. M. Itoh, and E. E. Haller, "Thermal conductivity of germanium crystals with different isotopic compositions," *Phys. Rev. B*, vol. 56, pp. 9431–9447, Oct 1997.

[2] R. L. Douglass, "Heat transport by spin waves in yttrium iron garnet," *Phys. Rev.*, vol. 129, pp. 1132–1135, Feb 1963.

[3] D. Walton, J. E. Rives, and Q. Khalid, "Thermal transport by coupled magnons and phonons in yttrium iron garnet at low temperatures," *Phys. Rev. B*, vol. 8, pp. 1210–1216, Aug 1973.

[4] R. Chisnell, J. S. Helton, D. E. Freedman, D. K. Singh, R. I. Bewley, D. G. Nocera, and Y. S. Lee, "Topological magnon bands in a kagome lattice ferromagnet," *Phys. Rev. Lett.*, vol. 115, p. 147201, Sep 2015.

[5] W. Schweika, M. Valldor, and P. Lemmens, "Approaching the ground state of the kagomé antiferromagnet," *Phys. Rev. Lett.*, vol. 98, p. 067201, Feb 2007.

[6] S. G. Tamilselvam, N. Panwar, S. Khare, R. Aralikatte, A. Sankaran, and S. Mani, "A visual programming paradigm for abstract deep learning model development," in *Proceedings of the 10th Indian Conference on Human-Computer Interaction*, IndiaHCI '19, (New York, NY, USA), Association for Computing Machinery, 2019.

[7] F. Rosenblatt, "The perceptron: A probabilistic model for information storage and organization in the brain.," *Psychological Review*, vol. 65, no. 6, pp. 386–408, 1958.

[8] T. Xie and J. C. Grossman, "Crystal graph convolutional neural networks for an accurate and interpretable prediction of material properties," *Phys. Rev. Lett.*, vol. 120, p. 145301, Apr 2018.

[9] J. Nelson and S. Sanvito, "Predicting the curie temperature of ferromagnets using machine learning," *Phys. Rev. Materials*, vol. 3, p. 104405, Oct 2019.

[10] D. J. Sanders and D. Walton, "Effect of magnon-phonon thermal relaxation on heat transport by magnons," *Phys. Rev. B*, vol. 15, pp. 1489–1494, Feb 1977.

[11] H. Sato, "On the Thermal Conductivity of Ferromagnetics," *Progress of Theoretical Physics*, vol. 13, pp. 119–120, 01 1955.

[12] B. Lüthi, "Thermal conductivity of yttrium iron garnet," *Journal of Physics and Chemistry of Solids*, vol. 23, no. 1, pp. 35–38, 1962.

[13] M. Akazawa, M. Shimozawa, S. Kittaka, T. Sakakibara, R. Okuma, Z. Hiroi, H.-Y. Lee, N. Kawashima, J. H. Han, and M. Yamashita, "Thermal hall effects of spins and phonons in kagome antiferromagnet cd-kapellasite," *Phys. Rev. X*, vol. 10, p. 041059, Dec 2020.

[14] M. Hirschberger, R. Chisnell, Y. S. Lee, and N. P. Ong, "Thermal hall effect of spin excitations in a kagome magnet," *Phys. Rev. Lett.*, vol. 115, p. 106603, Sep 2015.

[15] I. Ritchey, P. Chandra, and P. Coleman, "Spin folding in the two-dimensional heisenberg kagomé antiferromagnet," *Phys. Rev. B*, vol. 47, pp. 15342–15345, Jun 1993.

[16] P. W. Anderson, "More is different," *Science*, vol. 177, no. 4047, pp. 393–396, 1972.

[17] A. P. Ramirez, "Strongly geometrically frustrated magnets," *Annual Review of Materials Science*, vol. 24, no. 1, pp. 453–480, 1994.

[18] T. A. Kaplan, "Frustrated classical heisenberg model in one dimension with nearest-neighbor biquadratic exchange: Exact solution for the ground-state phase diagram," *Phys. Rev. B*, vol. 80, p. 012407, Jul 2009.

[19] M. Mezard, G. Parisi, N. Sourlas, G. Toulouse, and M. Virasoro, "Nature of the spin-glass phase," *Physical Review Letters - PHYS REV LETT*, vol. 52, pp. 1156–1159, 03 1984.

[20] K. Kanô and S. Naya, "Antiferromagnetism. The Kagomé Ising Net," *Progress of Theoretical Physics*, vol. 10, pp. 158–172, 08 1953.

[21] G. H. Wannier, "Antiferromagnetism. the triangular ising net," *Phys. Rev.*, vol. 79, pp. 357–364, Jul 1950.

[22] J. R. Stewart, G. Ehlers, H. Mutka, P. Fouquet, C. Payen, and R. Lortz, "Spin dynamics, short-range order, and spin freezing in $Y_{0.5}ca_{0.5}baco_4o_7$," *Phys. Rev. B*, vol. 83, p. 024405, Jan 2011.

[23] M. Valldor, "Remnant magnetization above room temperature in the semiconductor y0.5ca0.5baco4o7," *Solid State Sciences*, vol. 8, no. 11, pp. 1272–1280, 2006.

[24] N. Nagaosa, J. Sinova, S. Onoda, A. H. MacDonald, and N. P. Ong, "Anomalous hall effect," *Rev. Mod. Phys.*, vol. 82, pp. 1539–1592, May 2010.

[25] Isamu Akasaki, Hiroshi Amano, Masahiro Kito, and Kazumasa Hiramatsu, "Photoluminescence of mg-doped p-type gan and electroluminescence of gan p-n junction led," *Journal of Luminescence*, vol. 48-49, pp. 666 – 670, 1991.

[26] J. G. Bednorz and K. A. Müller, "Possible hightc superconductivity in the ba-la-cu-o system," *Zeitschrift für Physik B Condensed Matter*, vol. 64, no. 2, pp. 189–193, 1986.

[27] R. G. Parr, "Density functional theory of atoms and molecules," in *Horizons of Quantum Chemistry* (K. Fukui and B. Pullman, eds.), (Dordrecht), pp. 5–15, Springer Netherlands, 1980.

[28] K. T. Butler, D. W. Davies, H. Cartwright, O. Isayev, and A. Walsh, "Machine learning for molecular and materials science.," *Nature*, vol. 559, pp. 547–555, Jul 2018.

[29] K. Kanô and S. Naya, "Antiferromagnetism. The Kagomé Ising Net," *Progress of Theoretical Physics*, vol. 10, pp. 158–172, 08 1953.

[30] S.-Y. Louis, Y. Zhao, A. Nasiri, X. Wang, Y. Song, F. Liu, and J. Hu, "Graph convolutional neural networks with global attention for improved materials property prediction," *Phys. Chem. Chem. Phys.*, vol. 22, pp. 18141–18148, 2020.

[31] A. Jain, S. P. Ong, G. Hautier, W. Chen, W. D. Richards, S. Dacek, S. Cholia, D. Gunter, D. Skinner, G. Ceder, and K. a. Persson, "The Materials Project: A materials genome approach to accelerating materials innovation," *APL Materials*, vol. 1, no. 1, p. 011002, 2013.

[32] A. E. Hassanien, M. Tolba, and A. T. Azar, *Advanced Machine Learning Technologies and Applications: Second International Conference, AMLTA 2014, Cairo, Egypt, November 28-30, 2014*. Springer Publishing Company, Incorporated, 2014.

[33] M. C. Swain and J. M. Cole, "Chemdataextractor: A toolkit for automated extraction of chemical information from the scientific literature," *Journal of Chemical Information and Modeling*, vol. 56, no. 10, pp. 1894–1904, 2016. PMID: 27669338.

[34] S.-Y. Louis, Y. Zhao, A. Nasiri, X. Wang, Y. Song, F. Liu, and J. Hu, "Graph convolutional neural networks with global attention for improved materials property prediction," *Phys. Chem. Chem. Phys.*, vol. 22, pp. 18141–18148, 2020.